International Journal of Earth Sciences (2022) 111:929–948
https://doi.org/10.1007/s00531-022-02159-4

ORIGINAL PAPER

Non-uniform B-spline curve analyses of sigmoid brittle shear *P*- and ductile shear *S*-planes

Tuhin Biswas[1] · **Soumyajit Mukherjee**[1]

Received: 30 September 2020 / Accepted: 4 January 2022 / Published online: 17 February 2022

Abstract
Ideal morphologic representation of geologic structures using standard curves/surfaces can have far-reaching implications in estimating resources. From NW Lesser Himalaya (Uttarakhand state, India), field photographs of fully developed sigmoid-shaped brittle shear *P*- and ductile shear *S*- planes that crop out on the NW–SE (sub)vertical natural sections of rocks are matched by drawing curves using the B-spline tool in Rhinoceros software 5 SR service in 2D. These curves are advantageous to handle since the user can control their degrees, the control points are not the deciding factors, and that local modifications in shapes are permitted, unlike the Bézier curves. Sigmoid shapes are analyzed in detail using six shape parameters (lengths in between control points: L_1, L_2 and L_3; angles in between control points: α_1, α_2 and α_3). Good correlations between L_3 vs. L_1, L_2 vs. L_3 and L_1 vs. L_2 reveal the relation between wavelength (λ) and amplitude of the sigmoids that are classified into four types. Strong correlation between α_2 vs. α_3 and (α_3−α_1) vs. (α_1− α_2) suggest only the Type I, II and III sigmoids possess 180° rotational symmetry. Regression models (R^2 values) demonstrate that the sigmoid geometries are governed by (1) pre-existing or co-evolving regional structures and (2) lithologic composition.

Keywords Structural geology · Tectonics · Resource · Geometry of structures · Simple shear · Pure shear · Brittle shear

Introduction

Ductile and brittle shear zones in meso- and micro-scales commonly display sigmoid-shaped sheared rock masses/bulges/pods/mineral(s) (reviews in Passchier and Trouw 2005; Davis et al. 2010). In ductile shear zones these are commonly bound by the primary shear C-planes. Their sigmoid margins define the S-surface (e.g., Passchier and Trouw 2005; Fig. 1b of Dutta and Mukherjee 2019). Ponce et al. (2013) used the word "lozenge" to represent a number of shapes in bulged rocks in ductile shear zones (review in Mukherjee 2017). One of the shapes of these lozenges is sigmoid. The sigmoid-shape can also be defined by sheared quartz veins either in a train (e.g., Fig. 4d of Mukherjee and Koyi 2010) or being rootless (e.g., Fig. 4b of Mukherjee and Koyi 2010). At the micro-scale, ductile sheared rocks commonly display sigmoid-shaped mineral fish (Passchier and Trouw 2005; Mukherjee 2011).

In brittle shear zones, sigmoids are usually bound by the *Y*-planes and their sigmoid/lensoid margins themselves define the *P*-planes (e.g., Passchier and Trouw 2005; Fig. 2I of Dutta and Mukherjee 2019). Sigmoids in brittle shear zones can either be thrust slices (e.g., Fig. 3h in Li et al. 2017) or a part of rock masses inside the fault zone/fault gouge as step-overs or oversteps (Ahlgren 2001; Fig. 7d in Mukherjee 2013). Both in a ductile and a brittle shear zone, further deformation- most notably fracturing (Gudmundsson 2011) distort the sigmoid geometries. The sizes of the sigmoid masses can vary significantly in field even in close proximity.

Understanding and mathematical representation of geometries of geologic structures is one of the fundamental exercises in structural geology, which can have long-term implications in exploration studies, e.g., in predicting structural continuation in sub-surface (such as extrapolation of fold geometry by Busk method). A number of articles exist in this direction regarding folds (e.g., review in Fossen 2016; Gogoi and Mukherjee 2019),

✉ Soumyajit Mukherjee
soumyajitm@gmail.com; smukherjee@iitb.ac.in

Tuhin Biswas
tbtuhin24@gmail.com

[1] Department of Earth Sciences, Indian Institute of Technology Bombay, Powai, Mumbai 400 076, Maharashtra, India

joints/ fractures (Anders et al. 2014), and faults (Torabi et al. 2019). Geometric characterization of structures is a fundamental exercise in structural geology. Contrarily, geometric studies on sigmoid sheared structures have been scanty. Only ten Grotenhuis et al. (2003) and Mukherjee (2011) plotted graphs of aspect ratios of mineral fish vs. their local orientation/inclination to the primary shear *C*-planes. Later workers also defined few morphologic terms for such sheared objects. Passchier and Trouw (2005) in their Fig. 5.35 presented a 3D SEM image of a ductile sheared sigmoid mica grain.

Using Bézier and Non-Uniform B-spline (NURB) curves to model geometries of structures, most notable folds, have become popular in 2D (e.g., Gogoi et al. 2017; review in Nabavi and Fossen 2021) and also in 3D (Gogoi and Mukherjee 2019). Such curve fittings are usually rapid and can take care of a large number of fold geometries easily. Following this trend, this work fits B-spline curves to constrain the morphologies of the brittle and ductile-sheared sigmoids. The NURB curves are advantageous over the Bézier curves. This is because changes the control point locations affect the local segment of the NURB curves without disturbing their overall geometries, thus having finer shape control than the Bézier curve. In other words, NURB curve is advantageous since it gives more localized control over the produced curve and requires minimum assistance on the degree, smoothness and domain partition.

Sigmoid *P*-planes (and *S*-planes) are documented that envelope within the primary shear *Y*-planes (and *C*-planes) from the Uttarkashi-Mussoorrie transect of the Indian western Lesser Himalaya. Four types of shears are identified form field: (1) top-up-to-the-NW and (2) top-up-to-the-SE shears demonstrating a compressional stress regime, whereas, (3) top-down-to-the-NW and (4) top-down-to-the-SE an extensional one. This article also investigates the relation between the *P*- and *S*-plane geometries with stress regime (compressional/ extensional), lithology, and pre-existing or co-evolving regional structures.

The aim of the work is to introduce a new simple classification scheme to categorize commonly occurring sigmoid shape in brittle and ductile regime. The categorization communicates with conceptual understanding of naturally occurring sigmoids. The approach introduces two new parameters, rock lithology and regionally deformed rock to standardize the process. This has implications for brittle and ductile deformation modelling.

Non-uniform B-spline function

Fundamentals

Non- uniform B-spline curve is a polynomial curve termed by Schoenberg (Prautzsch et al. 2002 and references therein) that can be generated by $(n+1)$ number of control points and the B-spline basis function of degree k, in variable u. Such graphic design function is available in most of the photo-editing, 3D modelling and animation software (e.g., Corel Draw, Rhino, Motion, Final cut pro, Creo, Fushion 360°, TinkerCAD, BobCAD-CAM, SOLIDWORKS, MATLAB, CANVAS).

The B-spline curves are a combination of multiple segmented curve sections, which is continuous between the start and the end points (Fig. 1). Such curves can be either symmetric or asymmetric with respect to 180° rotational symmetry (Fig. 1). The significant advantage of this particular curve is that the degree of the curve (k) is user-defined and is independent of the control points. Thus, with multiple control points, e.g. ≥ 10, k can still be 3 or 4 as per the user. This is unlike the Bézier curve where the control points and k are inter-related: for 10 control points $k=10$ for the Bézier curves. A complex B-spline basis function is generated with increase in k. For $k=10$, the generated polynomial functions are u^9, u^8,…u. In B-spline curves, a particular segment is only controlled by a limited number of control points and thus provides a more precise local control leading to a better curve fitting.

The Non-Uniform B-spline curve can be written as:

$$P(u) = \sum_{i=0}^{n} P_i B_{i,k}(u), \quad (0 \le u \le n-k+2) \tag{1}$$

Here 'n' is a representation of control point, in which the total control points are $n+1$.

$B_{i,k}$:basis function of variable u and the parameter. It ranges from 0 to $(n-k+2)$.

For example, for four control points $(n+1=4)$, n equals 3. Let the degree of the curve be chosen as $k=3$.In this case, $B_{i,k}$ ranges from 0 to $n-k+2$, i.e., from 0 to 3–3 + 2 = 2.

The expression "$n-k+2$" defines the number of total segments within the B-spline curve. In the above example, the total number of segments are 2 (= 3–3 + 2). Segment 'r' ranges from $u=0$ to 1 and segment 's' from $u=1$ to 2 (Fig. 1). The deep violet square in Fig. 1 represents the meeting point of the curve segments 'r' and 's'.

Even though as per Eq. (1), all the control points are presumably involved to generate the curve, for a given range of u, some of the basis functions become zero. This assists the user to modify the curve especially at the edges.

Considering the curve segment-r (Fig. 1), the number of control points influencing the segment equals k. This means that the segment r is only influenced by P_0, P_1 and P_2, and not by P_3. Similarly, for segment 's', the control point P_0 has no influence and is only controlled by P_1, P_2 and P_3.

The term "Non-uniform" is used as the prefix to the "B-Spline Function" since not all the control points equally influence the curve segments. For example (Fig. 1), P_0 and P_3 can only influence the segment 'r' and

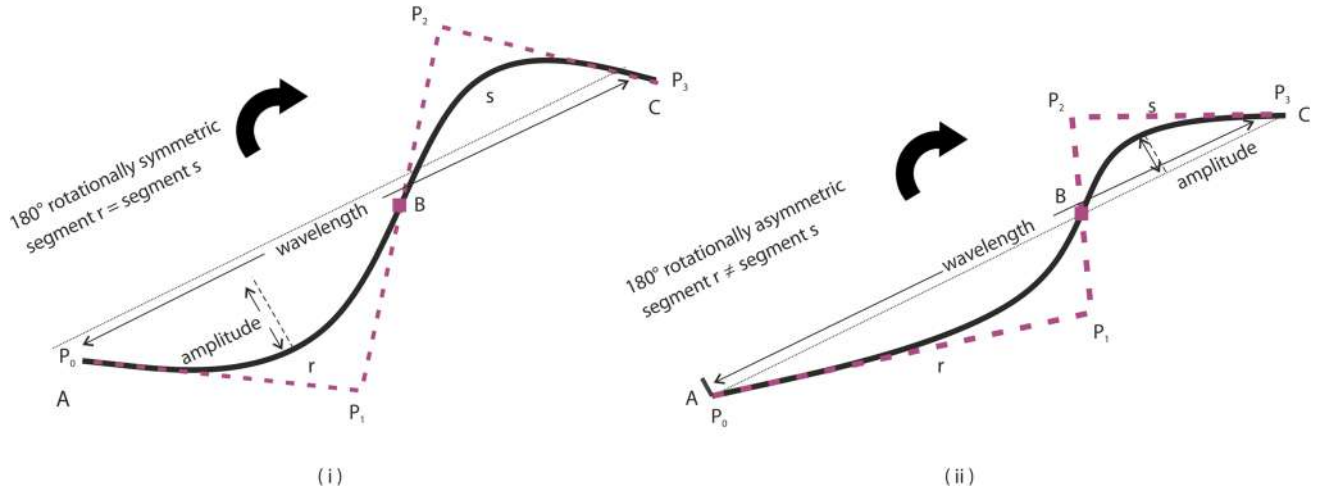

Fig. 1 Sigmoids generated using B-spline tool, in which P_0, P_1, P_2 and P_3 are the control points. Curve segments are represented by 'r' and 's'. Wavelength and amplitude are shown by arrows. Sigmoid are divided with respect to 180° rotational symmetry. **i** Symmetric: Sigmoid ('r' + 's') after 180° rotation appears exact same (segment 'r' = segment 's'). **ii** Asymmetric: Sigmoid ('r' + 's') after 180° rotation, clockwise or anticlockwise, appears different (segment 'r' ≠ segment 's')

's', respectively. However, P_1 and P_2 can influence both 'r' and 's' segments. Control points with uniform influence on the curve disable the curve to coincide with the starting point and the end point.

The continuity of the curve is defined by the magnitude of k. The curve has $C^{(k-2)}$ continuity. For $k=2$, the curve is C^1, or it has a slope continuity. For $k=2$, it is C^2, or it has a curve continuity.

Putting $n=k=3$ in Eq. (1):

$$P(u) = P_{0,3}(u)x_0 + P_{1,3}(u)x_1 + P_{2,3}(u)x_2 + P_{3,3}(u)x_3 \quad (0 \le u \le 2) \tag{2}$$

For $u=0$, 1; the non-zero B-spline basis function:

$$P(u) = P_{0,3}(u)x_0 + P_{1,3}(u)x_1 + P_{2,3}(u)x_2 \quad (0 \le u \le 1)$$

For $u=1$, 2, the non-zero B-spline basis function:

$$P(u) = P_{1,3}(u)x_1 + P_{2,3}(u)x_2 + P_{3,3}(u)x_3 \quad (1 \le u \le 2)$$

Inputs required to define a non-uniform B-spline curve are: (1) location of the control point (x, y, z co-ordinate in 3D), and (2) the order of the curve. For example, considering control points $(n+1)=4$, $n=3$; (Fig. 1), the ith control point is $P_{(i-1)}(x_{i-1}, y_{i-1}, z_{i-1})$ $\{i=1, 2, 3, 4\}$. The order (k) of the curve is 3.

Using B-spline tool in the Rhinoceros software (ver. 5, 2017) with the help of four control points and by defining the order of the curve ($k=3$), curve ('$r+s$') can be generated (Fig. 1).

Mathematical expression of the Basis-function

The Basis-function, $B_{i,k}(u)$ from Eq. (1), is defined as:

$$B_{i,k}(u) = \frac{u-t_i}{t_{i+k-1}-t_i}B_{i,k-1(u)} + \frac{t_{i+k}-u}{t_{i+k}-t_{i+1}}B_{i+1,k-1(u)} \quad \text{(De Boor 1972)} \tag{3}$$

Here t_i is the "knot vector" defined in the parameter space of the generated curve. The vector determines the start and stop of the polynomials of the drawn curve. The t_i function decides where and how the control points affect the generated curve.

Total number of$t$values can be expressed by$t : t_i(0 \le i \le n+k)$ (4)

The knot vectors are defined as:

$$t_i = 0 \text{ if } i < k; \tag{5}$$

$$t_i = i-k+1 \text{ if } k \le i \le n; \tag{6}$$

$$t_i = n-k+2 \text{ if } i > n \tag{7}$$

To find the basis function $B_{i,k}(u)$, the previous basis function $B_{i,k-1}(u)$ value is required. Thus, the B-spline basis function is also known as the recursive function (Cox 1972; De Boor 1972).

The recursive function terminates at:

$$B_{i,k}(u) = \begin{cases} 1, & \text{if } t_i u t_{i+1} \\ 0 & \text{otherwise.} \end{cases} \tag{8}$$

For $n=k=3$ (Fig. 1), the knot values (t_i, $0 \le i \le 6$) are $t_i=\{0, 0, 1, 2, 2, 2\}$.

To pass the curve through the end control points (e.g., P_0 and P_3 in Fig. 1), the influence of knot vectors at the edges should differ from those present at the middle (P_1 and P_2 in Fig. 1). Such non-uniform influence of knot vectors within the curve gives rise to the term "Non-Uniform Basis Function" (NUB curve).

Non-uniform rational basis-function (NURB curve)

The Non-Uniform Rational Basis-functions (NURB function) can be expressed as a modification/rational version of the B-spline curve:

$$P(u) = \sum_{i=0}^{n} P_i B_{i,k}(u) h_i \text{ where } 0 \le u \le n - k + 2 \quad (9)$$

Here "h" represents the weight of the control points. This enables any particular control point(s) to influence the entire curve more. In other words, the curve can be pulled more towards few particular control point(s).

Curves with three or more control points can be (re)generated and modified quickly based on the user's requirement of curve fitting using the B-spline tool in any photo-editing software viz., CAD, CAM and CAE.

Study area

Geology

Near-vertical rock sections along the National Highway-34 and the State Highway-30 were studies for ~ 152 km in the NW Lesser Himalaya (LH): from ~ 10 km NE of Uttarkashi towards Mussoorie (Uttarakhand, India) (Fig. 2). In absence of lineations related to ductile shear in the field, we have worked with sigmoids documented on ~ NW–SE natural rock sections. Eventually, the sigmoids have been documented on planes almost perpendicular to the line of intersection between the *P* or the *S*-planes defined by these sigmoid margins and the primary shear planes that bound them. If in any terrain, lineations are documents, *XZ*-sections must be observed for the sigmoids. Since we restrict to only geometric analyses of sigmoids and perform neither (1) kinematic analyses of shear zone, nor (2) tectonics of the orogen, the approximate planes chosen in this study do not affect (1) and (2). Bound by the Siwalik range in the south and the Greater Himalayan Crystallines in the north, the LH is a Paleoproterozoic–Paleozoic sedimentary succession (review in Célérier et al. 2009; Biswas et al. 2021). More accurately, the LH is bound at south by the Main Boundary Thrust and at the north by the Main Central Thrust (MCT) zone. In field the followings rocks are encountered: schists, phyllites, slates, quartzites, dolomites, conglomerates and limestones. Overall, LH is characterized by low-grade greenschist metamorphic facies. North of the Sainj village, amphibolite facies rocks and granite-gneisses are found in the MCT zone (Bose and Mukherjee 2019a). Repository Table 1 in ESM compiles the stratigraphy of the area based on previous literatures.

Structures and geochronology

The cooling age of LH units, based on $^{40}Ar/^{39}Ar$ dating of white micas, ranges 4.3–6.7 Ma (Thiede et al. 2005). Young dating age of 4–7 Ma recorded in between the Munsiari Thrust and the MCT zone in the Sutlej valley (Himachal Pradesh, India, Vannay et al. 2004). The Munsiari Thrust activated ~ 19.8 ± 2.6 Ma (Ar/Ar dating on hornblende; Metcalfe 1993). However, Th–Pb monazite dating of Catlos et al. (2002) gave 5.9 ± 0.2 Ma as the time of activation. Montemagni et al. (2020) deduced a much younger Ar–Ar age of 5–4 Ma from the Munsiari Thrust in the Garhwal Himalaya. The thrust separating the Inner Lesser Himalaya in the north from the Outer Lesser Himalaya in the south has been recognized variously as the Tons Thrust/Srinagar Thrust/North Almora Thrust (review in Bose and Mukherjee 2019a). The Berinag Thrust slipped top-up-to-the-SW and later folded (Bose and Mukherjee 2019a) within the Inner Lesser Himalaya. The Singuini Thrust is equivalent of the Khattukhal Fault (Agarwal and Kumar 1973) and coincides with the axial trace the Khattukhal Anticline. Dharasu Thrust/Nalupani fault/Dharkot Dislocation (review in Agarwal and Kumar 1973) lies south of the Singuini Thrust. The Tons Thrust at the margin between the Inner- and the Outer Lesser Himalaya reactivated ~ 14 Ma as a back-thrust (Patel et al. 2015; Agarwal et al. 2016). The Outer Lesser Himalaya consists of few major tectonic units: the Mussoorie syncline possesses ~ northern dipping Aglar Thrust and ~ southern dipping Basul Thrust (Jain 1971). The Kathu-ki-chail Thrust passes through the Mussoorie synclinal axis that reactivated during the Himalayan compression (Dubey 2014). The MBT activated ~ 9–11 Ma (apatite fission track dating: Meigs et al. 1995; Thakur et al. 2014).

Ductile and brittle shears with orogen–perpendicular sense of shear have already been studied extensively from the LH along the natural (sub)vertical NE–SW rock-sections by the previous workers (e.g., Mukhopadhyay and Mishra 2005; Célérier et al. 2009; Agarwal et al. 2016; Bose and Mukherjee 2019a, b; Mahato et al. 2019). However, shear structures observed on the orogen-parallel NW–SE sections received far less attention.

Onset of Tibet and Himalayan orogen-parallel extension (Repository Fig. 1 in ESM) is estimated between 15 and 5 Ma by various authors. For example, $^{40}Ar/^{39}Ar$ thermochronology on muscovites at the upper Karnali valley

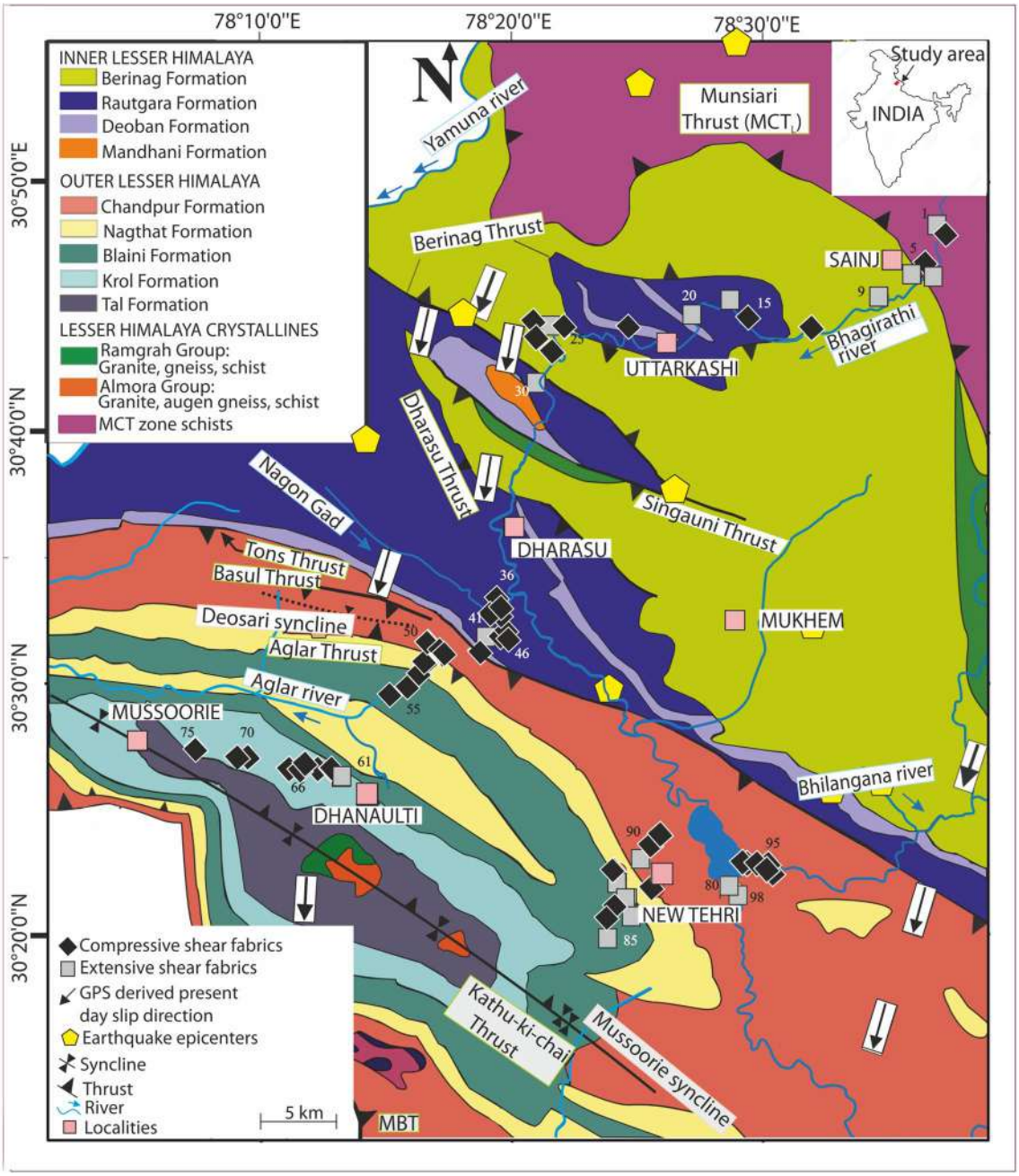

Fig. 2 Shear fabric documented along NW–SE trend located in the geological map of the Garhwal Lesser Himalaya. The map along with the compiled structural and tectonic information is taken from Bose and Mukherjee (2019a)

(Nepal) indicates an extension ~ 15–13 Ma (Nagy et al. 2015). Hintersberger et al. (2011) recorded brittle-ductile transition between 15 and 17.5 Ma from the NW Greater Himalayan rocks and also the NW–SE extension. This extension (D_4), supposedly equivalent with NE–SW compression (D_1), prevailed between 12 and 11 Ma (zircon fission track date: Vannay et al. 2004). Based on the cross-cut relationship between the Khula Kangri granite (12.5 Ma) and the South Tibetan Detachment (STD), Edward and Harrison (1997) estimated initiation of orogen-parallel extension to be ~ 10 Ma. Repository File 1 reviews orogen-parallel shear from Tibet.

Agarwal and Kumar (1973) and subsequently Jain (1987) identified orogen-parallel compression/NW–SE compression to be younger than the NE–SW compression (D_1 of Hintersberger et al. 2011). In the NW LH, a D_3 NE–SW extension

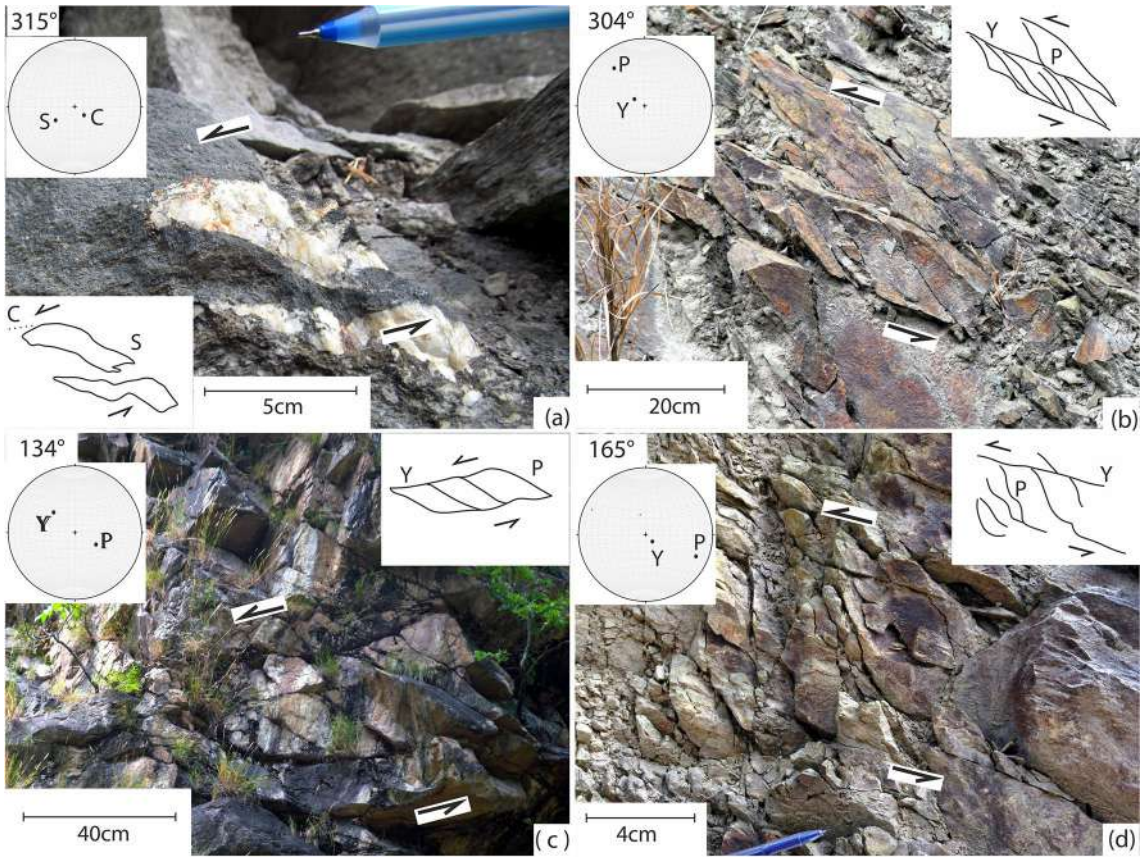

Fig. 3 Field evidence of orogen-parallel extensional and compressional shear fabrics documented in the NW Lesser Himalaya along the Dehradun-Uttarkashi transect. Dip amount/dip direction: *x*°/*y*°. **a** Within Main Central Thrust (MCT) zone, sigmoid *S*-planes (29°/55°) bounded by *C*-planes (not visible; 16°/315°) records top-down-to-the-NW extensional shear by quartz-fish within low-grade metamorphic schist. Location 5 in Fig. 2. **b** Brittle shear indicating top-up-to-the-NW compressional shear in Rautgara schist (*Y*-plane: 15°/124°; *P*-plane: dip amount/dip direction: 60°/140°). **c** Location 36 in Fig. 2c Berinag Quartzite affected by top-down-to-the-SE extensional brittle shear zones with well-developed *Y*- (36°/134°) and *P*-planes (30°/300°). Location 29 in Fig. 2d. **d** Fragmented *P*-planes bordered by segmented *Y*-planes denote top-up-to-the-SE compressional shear, within the Rautgara schists. *Y*-plane: 25°/165°, *P*-plane: 77°/115°. Location 5 in Fig. 2

as per Hintersberger et al. (2011) is presumably correlated with the NW–SE compression suggesting a deformation around 7–4 Ma (^{40}Ar/^{39}Ar dating).

Top-up-to-the-NW and top-up-to-the-SE (compressional shear fabric), and top-down-to-the-NW and top-down-to-the-SE (extensional shear fabric) shears are photographed in this work from the NW–SE natural cross-sections (Fig. 3). The shears are deciphered from S-C fabric and brittle shear planes *Y* and *P*, from total 98 spots. Several earlier workers (e.g., reviews in Yin 2006; Bose and Mukherjee 2019a) completely missed these deformations. A total of 103 curved *S*-(and *P*-) planes bound by *C*- (and *Y*-) planes are considered. Amongst these, 67 curves (*P*-planes) belong to the Inner Lesser Himalaya, and 27 (*P*-planes) to the Outer Lesser Himalaya. Nine curves (*S*-planes) come from the MCT zone schist. Where sigmoid *P*- and *S*-planes are incompletely developed or are broken naturally (Repository Fig. 2 in ESM), we avoided them in the present work.

Methods

Usually to generate the exact shape of the sigmoid curves, this work satisfactorily uses four control points. A good fit is understood visually. The degree is fixed to $k=3$ to achieve the desired degree of smoothness. With increase in k value the order of the curve increases**.** For example, if $k=4$, a cubic degree (u^3) of polynomial forms. With decreasing k values, the order of the curve decreases and the overall curvature closes near the control points: for $k=2$, linear, and worse, for $k=1$, no curve is simulated. The chosen degree smoothens the curve and avoids complex polynomial equations involving u^4, u^5, u^6 etc. Summarily, having less control points make the fit unsatisfactorily. On the other hand more than 4 control points do not augment the fit significantly.

The B-spline curve can fit with the sigmoid using the Rhinoceros software 5 SR Service (free trial version) as follows (Figs. 4, 5):

Fig. 4 Top-up-to-the-NW brittle shear, within Rautgara Slate, Inner Lesser Himalaya, is defined by sigmoid-shaped *P*-plane, bound by two sub-parallel *Y*-planes. Inset stereo-plots of poles of *Y*- and *P*-planes. The inset line traces the right margin of the sigmoid

1. Import the digital field photograph image consisting of the curved shear plane (*P* or the *S*-plane) bound by a set of primary shear planes (*Y*- or the *C*-plane) in the Rhinoceros *XY*-graphical interface (Fig. 5a).
2. Rotate the image so that *Y*- or the *C*-plane parallels the abscissa (Fig. 5b).
3. Place the leftmost end points of the *P*- or the *S*-plane at the origin (0, 0) (Fig. 5c).
4. Draw a nearly matched curve of the *P*- or the *S*-plane using the B-spline graphic tool using four control points, starting from the origin of the curve. Fix two control points, P_0 and P_3, as the end points of the curve. Define the weight of the control points $(h) = 1$ so that all the control points have equal influence on the curve. Define the degree of the curve (here $k = 3$) allowing considerable smoothness (Fig. 5d).
5. Adjust the two control points (P_1, P_2) along *X*- and *Y*-axes in both the positive and the negative directions, and match the exact curve pattern. P_1, P_2 are the movable control points and its position generates the curvature of the sigmoid. By moving P_1 and P_2, location the drawn curve is visually matched with the field photograph. (Fig. 5e).
6. If the newly created curve exactly/reasonably replicates the P- or the S-plane as present in the imported picture, join all the controlling points (P_1, P_2 and P_3) from the origin or from P_0 and measure individual lengths (L_1, L_3 and L_2, respectively) (Fig. 5f).
7. Measure the angles $\alpha_1 = \angle OP_0P_1$, $\alpha_2 = \angle OP_0P_3$, and $\alpha_3 = \angle OP_0P_2$ (Fig. 5g).

The 180° rotational asymmetry of the curve (Fig. 1ii) manifested by different wavelengths (λ values) in its different segments can be accounted by changing the positions of P_1 and P_2 (Fig. 5d).

Various shapes and sizes of sigmoids are encountered in the field. Values of lengths L_i and angles α_i, $(i = 1, 2, 3)$, are utilized in a relative sense (e.g., "low L_1 value" means a much lower magnitude of L_1 with respect to L_2 and L_3) to understand the sigmoid geometry.

We regenerate/trace field-photographed *S*- and *P*-planes (few attitudes presented in Fig. 6) in computer using the Rhino 5 SR Service, a free computer-aided design with an in-built B-spline tool.

After bringing in the Rhino 5 SR Service platform, individual lengths of *P*- and *S*-curves were measured from origin (0,0) in the photographs in terms of L_1, L_2 and L_3 (Fig. 5h). The angles (α_1, α_2 and α_3) (Fig. 5h) are calculated (Table 1).

Stronger simple shear is expected to reduce α_2 and lengthen L_2 (Fig. 7; Mukherjee 2011). This work incorporates additional four parameters (α_1, α_3, L_1 and L_3; Fig. 5h), in which, along with α_2, acute angles α_1 and α_3 reduce similarly and L_1 and L_3 expand as shear continues. The article attempts to draw relations in between the six parameters (α_1, α_2, α_3, L_1, L_2 and L_3) to constrain the sigmoid geometry.

Results

General points

Using the B-spline tool, the redrawn curves from the field photograph can be defined in terms of six parameters (L_i, α_i; $i = 1, 2, 3$). These parameters were mutually compared in terms of "first order plots" (Table 2, sl. no. 1–4; Fig. 8i.–iv). Next, the parameters were used to calculate ratios and compared as the "second order plots" (Table 3; Fig. 9i). The best fit straight lines were derived from these plots along with their R^2 values. R is the linear correlation coefficient. R^2 is the statistical measurement of closeness of the data with the matched best fit line of regression.

Practically no correlation ($R^2 = 0.0003$) was noted between α_2 and L_2 (Table 2, sl. no. 5). Scatter plots support a moderate to good regression model fit (marked by '^' in Tables 2, 3, e.g., sl. no. 1, 2, 3 and 4 in Table 2 and sl. no.1 in Table 3).

The other first-order and the second-order plots suggest poor regression model fit (marked by '*' in Table 2, e.g., sl. no.5 in Table 2) between the chosen pair of parameters.

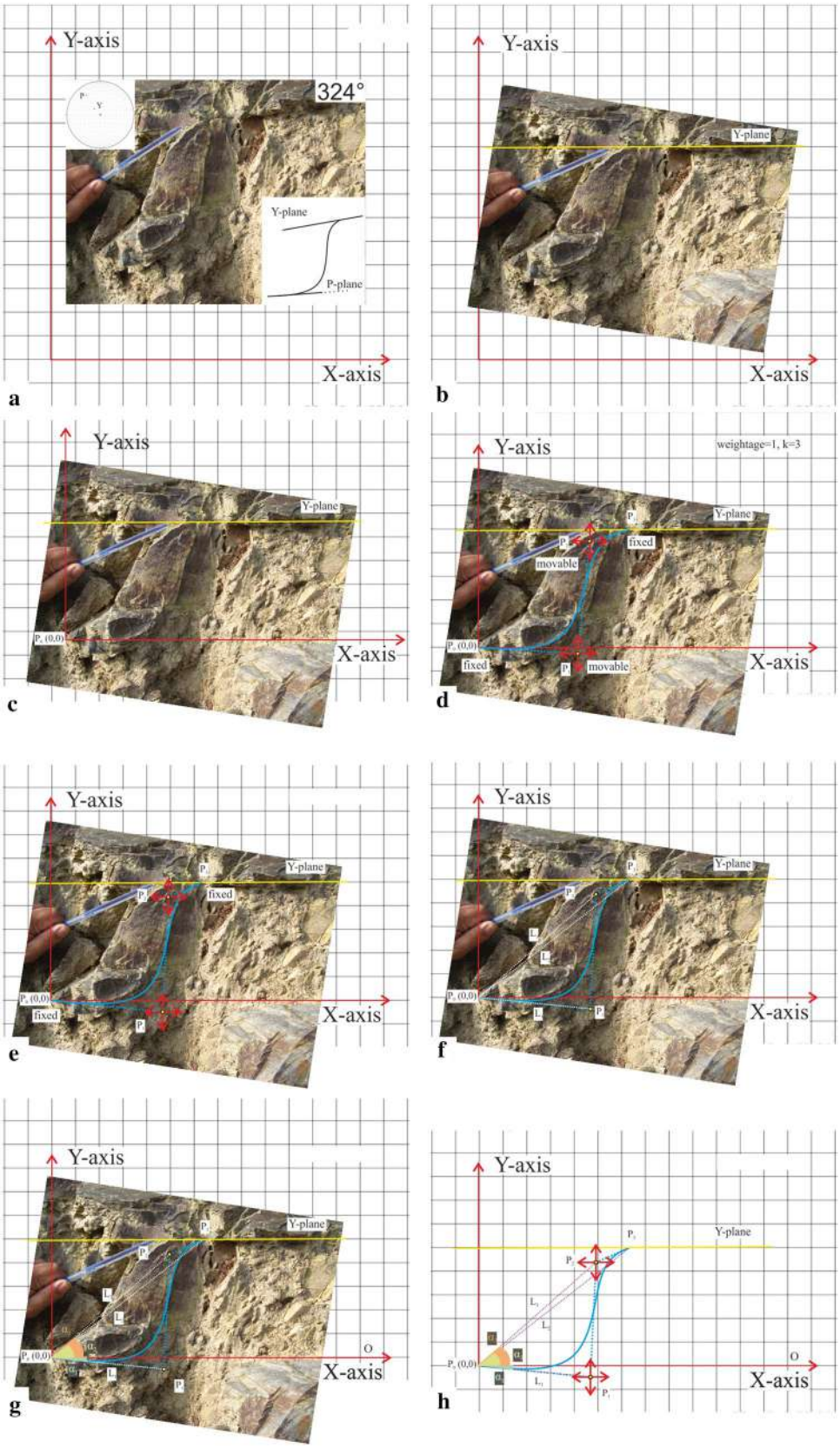

Fig. 5 P-plane regenerated using the Rhinoceros software. Parameters L_1, L_2, L_3, α_1, α_2 and α_3 are defined. **a** Import the digital field-snap in the graph. **b** Rotate the image so that the *Y*-shear plane parallels the abscissa. **c** Place left end points of the *P*-plane at origin (0,0). **d** Draw a nearly matched curve pattern of *P*-plane using the B-spline graphic tool with four control points from origin. P_0 and P_3 are the end points of the curve. Add weight of the control points = 1, degree of the curve, $k = 3$. **e** Adjust the two control points (P_1, P_2) along the *X*- and the *Y*- axes. **f** Join all the controlling points (P_1, P_2, and P_3) with the origin (P_0) and measure individual lengths (L_1, L_3, and L_2, respectively). **g** Measure the angles α_1, α_2 and α_3: $\angle OP_0P_1 = \alpha_1$, $\angle OP_0P_3 = \alpha_2$, $\angle OP_0P_2 = \alpha_3$. **h** Regenerated *P*-plane using B-spline tool visually matching with field photograph marked with blue color. *Y*-plane is marked with yellow color, which lies parallel with *X*-axis. P_0 and P_3 are the end points, whereas P_1 and P_2 (yellow circles) are the control points which can be moved till it matches with desired visual fitness. P_0P_1 marked as L_1, P_0P_3 represents L_2 and P_0P_2 marked as L_3. $\angle OP_0P_1 = \alpha_1$ marked with light green, $\angle OP_0P_3 = \alpha_2$ represented in yellow and $\angle OP_0P_2 = \alpha_3$ marked by orange

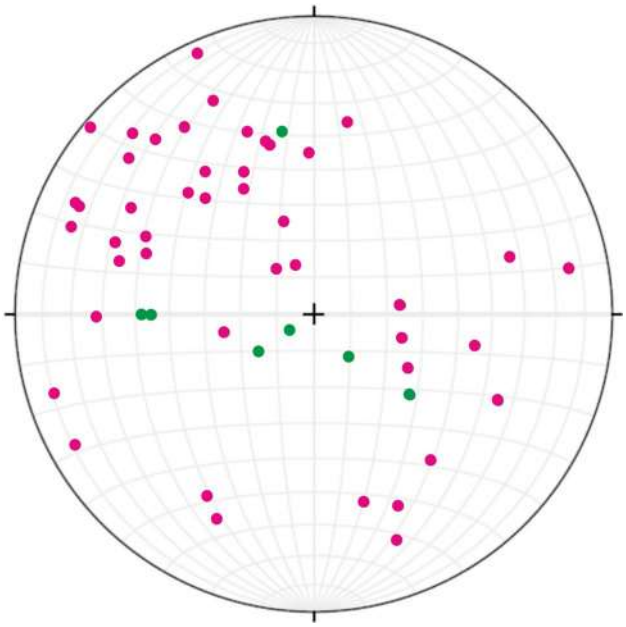

Fig. 6 Poles of seven *S*-planes marked by green and 45 *P*-planes pink dots in a stereo-net. Data collected from the NW Indian Lesser Himalaya

Types of sigmoids

Generally, for sigmoidal S and P planes (Fig. 3), two curve segments bulge in the middle, taper towards the end and are bound by ductile shear C-planes/brittle shear Y-planes. The sigmoid can be classified based on their wavelengths and amplitudes (Fig. 1) into the following four types.

Type-I The sigmoid curve is characterized by low amplitude and low wavelength showing very little curvature. Relative L_1 values are the lowest with very little difference between L_2 and L_3 values (Fig. 10i). Acute angles α_1, α_2 and α_3 are close-spaced magnitude-wise, and the sigmoid segment '*r*' after 180° rotation replicates the segment '*s*'. Thus the entire sigmoid can be stated to have a 180° rotational symmetry (Fig. 10ii).

Type-II This particular curve is defined by moderate wavelength and amplitude in which the L_1–L_2 and the L_1–L_3 values are more than those for the Type-I but less than those for the Type-III sigmoids (Fig. 10i). Acute angles α_1, α_2 and α_3 are equally spaced ($\alpha_2-\alpha_1 \approx \alpha_3-\alpha_2$) leading to 180° rotational symmetry of these sigmoids (Fig. 10ii).

Type-III This type of a curve has the maximum curvature thus having a very high relative L_1 and close to the values of L_2 and L_3 (Fig. 10i; explained in Repository Files 1 and 2 in ESM). Angles α_1, α_2 and α_3 differ much but $\alpha_2-\alpha_1 \approx \alpha_3-\alpha_2$ along with the maximum wavelength (L_2). Such sigmoids are symmetric after 180° rotation (Fig. 10ii).

Type-IV This type of a sigmoid is characterized by its asymmetry. The curve fails to regenerate itself after 180° rotation and thus segment '*r*' and segment '*s*' differ (Fig. 10ii). Here $\alpha_2-\alpha_1 \neq \alpha_3-\alpha_2$. Thus in ($\alpha_3-\alpha_1$) vs. ($\alpha_1$-$\alpha_2$) plot, the asymmetry leads the scatter plot points falling away from the regression line $R^2=1$.

Discussions

General points

Understanding of geologic structures using graphic tools (Bézier curve, NURB curve, GOCAD etc.) has gained popularity (e.g., Renard and Courrioux 1994; de Kemp and Sprague 2003; Zhong et al. 2004; Paluszny et al. 2007; Liu et al. 2009a, b; Hudleston and Treagus 2010; Gogoi and Mukherjee 2017). 2D understanding of geometry in meso as well as in micro-scale can further 3D graphical modelling to visualize, interpret and analyse geological structures (Zhong et al. 2004; Sprague and Kemp 2005; Gogoi and Mukherjee 2019). Such modelling can have long-term implications in engineering geology (e.g., Francké and Yelf 2003; Koerber et al. 2003; Zhong et al. 2006; Barazzetti et al. 2016; Jacquemyn et al. 2019).

Geometry and distribution of any structural elements are influenced by the stress regime, lithologic variation and existing regional structures (Fossen et al. 2017). Sigmoid shapes of shear fabrics depend on water fugacity, pure shear, simple shear, amount of strain, grain-size (e.g., Sonder, 2001; Bose et al. 2018). Meyer et al. (2017) suggested material heterogeneity to be the responsible factor to develop sigmoids and/or shear zones. Shear fractures and sigmoids indicate grain reorganization, cataclasis, and/or precipitation (Peacock et al. 2018 and references therein). Understanding of fracture/sigmoid geometry can be important to deduce the prevalent stress pattern, kinematics and temporal relationship in shear zones (Peacock et al. 2018; Liu et al. 2009b). Thus, geometric modelling of shear structures is essential (Hudleston and Treagus 2010).

Sigmoids encountered in the field ranges from mm to cm and sometimes to meter-scale. To understand the types of sigmoid the article emphasizes on length ration and angle ratio plots.

Several correlation plots in geology such as in geochemical composition (e.g., Fisher 1995; Akram et al. 2017; Evans et al. 2018), mechanical parameters (Akram et al. 2017), topographic features (Gabrielli and McDonnell 2020), heavy metal concentration (Huisman et al. 1997), soil chemistry (Maynard 1992) suggests that $R^2>0.5$ indicating moderate to strong correlation. In this study, in general, based on $R^2>0.5$ moderate-strong correlations are observed in L_3 vs. L_1 ($R^2=0.52$), L_2 vs. L_3 ($R^2=0.92$) and L_1 vs. L_2 ($R^2=0.59$). With relatively low L_1 values, little difference between L_2 and L_3 values indicates that the studied sigmoid shear planes,

Table 1 Total of 103 reproduced *P*- and *S*- plane parameters

Sl no	Formation/lithology	L_1 (mm)	L_2 (mm)	L_3 (mm)	α_1 (°)	α_2 (°)	α_3 (°)	Weight	Control points	Degree of Curve
1	Chandpur Slates	0.204	1.426	0.777	44.59	38.206	50.145	1	4	3
2	Chandpur Slates	1.035	2.542	1.788	36.394	38.459	55.896	1	4	3
3	Chandpur Slates	1.189	2.706	1.793	20.34	42.304	56.9	1	4	3
4	Rautgara Formation Slate	24.163	25.953	17.45	− 6.26	38.29	52.51	1	4	3
5	Rautgara Slates	9.423	27.575	21.702	7.91	24.72	29.62	1	4	3
6	Rautgara Slates	1.88	6.71	2.58	3.98	10.25	29.52	1	4	3
7	Rautgara Slates	1.527	14.906	8.665	50.054	28.899	59.144	1	4	3
8	Rautgara Slates	24.12	45.69	28.39	− 17.535	27.07	50.83	1	4	3
9	Rautgara Slates	13.758	36.05	27.83	− 6.83	23.495	29.81	1	4	3
10	Rautgara Slates	14.23	25.092	19.97	− 12.22	19.524	26.051	1	4	3
11	Rautgara Slates	3.271	11.31	8.51	− 12.9	21.72	35.043	1	4	3
12	Rautgara Slates	1.017	3.206	1.548	− 6.729	25.239	31.831	1	4	3
13	Rautgara Slates	1.101	3.425	2.38	− 5.318	19.92	36.495	1	4	3
14	Rautgara Slates	14.411	30.976	25.033	30.242	53.873	61.896	1	4	3
15	Rautgara Slates	6.011	24.963	22.302	18.881	65.671	80.056	1	4	3
16	Rautgara Slates	8.977	24.662	20.758	13.293	60.817	69.708	1	4	3
17	Rautgara Slates	2.115	9.76	6.28	45.27	68.48	88.905	1	4	3
18	Rautgara Slates	1.08	5.53	4.61	65.69	39.34	58.262	1	4	3
19	Rautgara Slates	3.16	8.99	7.53	− 2.55	61.75	72.68	1	4	3
20	Rautgara Slates	6.527	19.009	12.705	16.815	26.706	37.139	1	4	3
21	Rautgara Slates	5.303	14.554	13.483	22.035	30.546	35.198	1	4	3
22	Rautgara Slates	1.292	3.789	2.437	− 4.02	30.516	46.957	1	4	3
23	Rautgara Slates	5.441	22.926	19.803	4.234	20.92	24.719	1	4	3
24	Rautgara Slates	1.7	8.886	6.083	11.635	15.216	18.665	1	4	3
25	Rautgara Slates	5.417	20.336	16.611	15.742	23.869	25.622	1	4	3
26	Rautgara Slates	5.716	12.058	10.436	− 10.596	36.18	45.273	1	4	3
27	Rautgara Slates	4.842	8.311	5.465	− 5.69	45.975	79.895	1	4	3
28	Rautgara Slates	2.834	5.7	4.085	− 5.581	29.467	34.369	1	4	3
29	Rautgara Slates	2.974	7.075	4.448	11.05	36.343	46.534	1	4	3
30	Berinag Quartzite	5.1	10.66	6.514	− 2	41.36	48.16	1	4	3
31	Berinag Quartzite	1.23	3.02	1.65	− 2	28.8	38.29	1	4	3
32	Berinag Quartzite	21.71	39.887	25.448	− 12.77	9.77	16.51	1	4	3
33	Berinag Quartzite	14.11	40.55	29.75	− 13.75	34.261	43.97	1	4	3
34	Berinag Quartzite	11.65	24.04	17.619	− 5.089	12.06	16.59	1	4	3
35	Berinag Quartzite	6.85	20.93	17.15	− 16.13	31.57	41.48	1	4	3
36	Berinag Quartzite	4.78	8.15	5.67	− 2.05	29.14	34.86	1	4	3
37	Berinag Quartzite	4.285	9.948	7.754	− 24.07	22.68	36.57	1	4	3
38	Berinag Quartzite	2.817	9.486	6.221	0.8	17.912	20.913	1	4	3
39	Berinag Quartzite	7.768	18.592	12.965	− 3.274	14.34	25.97	1	4	3
40	Berinag Quartzite	1.91	7.04	3.12	− 24.53	24.47	29.62	1	4	3
41	Berinag Quartzite	1.736	5.225	3.531	− 18.243	16.078	31.015	1	4	3
42	Berinag Quartzite	0.718	4.503	2.696	− 16.368	16.06	32.538	1	4	3
43	Berinag Quartzite	1.014	4.883	3.293	− 2.595	36.048	46.641	1	4	3
44	Berinag Quartzite	9.18	20.37	8.324	14.608	28.779	62.324	1	4	3
45	Berinag Quartzite	3.817	12.215	7.866	16.535	35.297	52.95	1	4	3
46	Berinag Quartzite	0.824	7.162	3.825	24.313	40.243	79.998	1	4	3
47	Berinag Quartzite	6.179	30.201	19.407	10.571	22.289	42.098	1	4	3
48	Berinag Quartzite	0.675	1.443	0.954	6.462	33.588	53.458	1	4	3

Table 1 (continued)

Sl no	Formation/lithology	L_1 (mm)	L_2 (mm)	L_3 (mm)	α_1 (°)	α_2 (°)	α_3 (°)	Weight	Control points	Degree of Curve
49	Berinag Quartzite	0.477	5.11	4.092	23.971	32.713	42.796	1	4	3
50	Berinag Quartzite	1.435	4.117	3.722	17.621	30.209	35.974	1	4	3
51	Blaini Formation conglomerate clast	6.421	17.624	12.269	37.58	36.227	51.761	1	4	3
52	Blaini Formation conglomerate clast	7.009	14.903	11.127	6.326	41.869	57.393	1	4	3
53	Blaini Formation conglomerate clast	6.345	15.044	8.546	4.172	25.812	41.248	1	4	3
54	Krol Formation Limestone	6.021	11.4	8.37	− 4.96	53.641	77.332	1	4	3
55	Krol Formation Limestone	2.389	8.262	6.735	− 43.492	24.732	33.59	1	4	3
56	Krol Formation Limestone	3.486	6.859	5.464	− 2.3	29.978	42.634	1	4	3
57	Krol Formation Limestone	3.791	8.545	8.44	18.815	39.058	45.364	1	4	3
58	Krol Formation Limestone	9.864	17.641	15.274	− 7.942	3.79	9.678	1	4	3
59	Krol Formation Limestone	4.228	13.767	4.211	2.161	29.059	74.812	1	4	3
60	Krol Formation Limestone	7.971	11.578	10.801	− 8.149	23.045	27.921	1	4	3
61	Krol Formation Limestone	4.494	13.873	11.007	37.049	54.445	70.267	1	4	3
62	Krol Formation Limestone	4.26	12.081	9.244	14.036	54.59	65.719	1	4	3
63	Krol Formation Limestone	1.858	9.756	7.538	26.531	53.063	65.517	1	4	3
64	MCT zone Schist	14.8	30.75	21.6	5.63	28.65	46.09	1	4	3
65	MCT zone Schist	15.237	19.712	13.115	− 2.078	20.635	25.67	1	4	3
66	MCT zone Schist	3.21	26.22	21.08	− 1.16	33.29	46.49	1	4	3
67	MCT zone Schist	4.75	17.29	12.904	8.306	28.25	36.47	1	4	3
68	MCT zone Schist	0.834	30.487	14.356	15.945	20.243	58.951	1	4	3
69	MCT zone Schist	7.469	22.697	15.801	38.826	64.072	68.715	1	4	3
70	MCT zone Schist	8.043	29.144	26.014	10.955	69.278	75.37	1	4	3
71	MCT zone Schist	6.025	18.783	11.103	16.46	47.318	68.155	1	4	3
72	MCT zone Schist	4.977	14.636	11.909	24.22	45.442	58.707	1	4	3
73	Nagthat Quartzite	4.358	31.247	25.284	21.282	41.733	48.257	1	4	3
74	Nagthat Quartzite	2.282	12.988	9.06	− 13.001	29.88	35.512	1	4	3
75	Nagthat Quartzite	1.6288	7.553	6.056	8.781	35.761	41.087	1	4	3
76	Nagthat Quartzite	2.999	5.26	3.955	17.74	49.994	63.123	1	4	3
77	Nagthat Quartzite	1.331	4.257	2.962	31.529	40.825	57.145	1	4	3
78	Nagthat Quartzite	0.862	2.738	2.002	20.512	38.972	40.028	1	4	3
79	Nagthat Quartzite	4.702	10.892	13.757	31.393	55.259	46.493	1	4	3
80	Nagthat Quartzite	3.796	17.773	16.412	22.593	35.653	36.562	1	4	3
81	Nagthat Quartzite	0.466	31.936	26.892	0.138	31.415	34.372	1	4	3
82	Nagthat Quartzite	3.498	15.211	13.731	− 8.854	40.212	45.882	1	4	3
83	Nagthat Shaly Quartzite	5.161	16.81	12.56	1.63	23.44	26.316	1	4	3
84	Rautgara Quartzite	7.102	26.82	16.64	9.81	46.04	50.12	1	4	3
85	Rautgara Quartzite	7.436	24.879	17.39	9.5	47.3	62.628	1	4	3
86	Rautgara Quartzite	5.414	11.788	6.577	37.303	44.086	78.535	1	4	3
87	Rautgara Quartzite	2.502	10.311	6.514	28.727	39.894	60.058	1	4	3
88	Rautgara Quartzite	5.527	14.043	10.98	− 15.29	30.73	44.677	1	4	3
89	Rautgara Quartzite	1.84	5.55	3.85	1.72	45.731	67.479	1	4	3
90	Rautgara Quartzite	17.1	45.45	36.04	5.3	34.46	40.079	1	4	3
91	Rautgara Quartzite	1.66	6.21	4.25	13.113	30.58	48.57	1	4	3
92	Rautgara Quartzite	1.43	5.27	3.62	4.16	32.54	38.29	1	4	3
93	Rautgara Quartzite	0.49	1.785	1.442	− 8.319	42.13	54.38	1	4	3
94	Rautgara Quartzite	1.101	3.336	2.332	25.029	34.364	55.198	1	4	3
95	Rautgara Quartzite	6.662	27.868	23.317	9.653	32.922	40.587	1	4	3
96	Rautgara Quartzite	7.171	27.942	24.461	− 2.569	38.063	45.71	1	4	3

Table 1 (continued)

Sl no	Formation/lithology	L_1 (mm)	L_2 (mm)	L_3 (mm)	α_1 (°)	α_2 (°)	α_3 (°)	Weight	Control points	Degree of Curve
97	Rautgara Quartzite	7.169	21.253	18.905	− 1.948	39.129	42.054	1	4	3
98	Rautgara Quartzites	5.724	12.009	9.016	8.631	22.08	30.204	1	4	3
99	Rautgara Quartzites	1.563	11.81	6.839	26.951	26.998	37.781	1	4	3
100	Rautgara Quartzites	0.833	13.22	9.082	9.659	29.96	41.595	1	4	3
101	Rautgara Slates altered with Quartzite	3.26	11.1	8.1	7.562	25.9	50.46	1	4	3
102	Rautgara Slate altered with Quartzite	2.892	8.84	6.99	21.12	31.74	39.2	1	4	3
103	Rautgara Slate altered with Quartzite	2.7	6.07	3.49	− 14.48	23.64	30.88	1	4	3

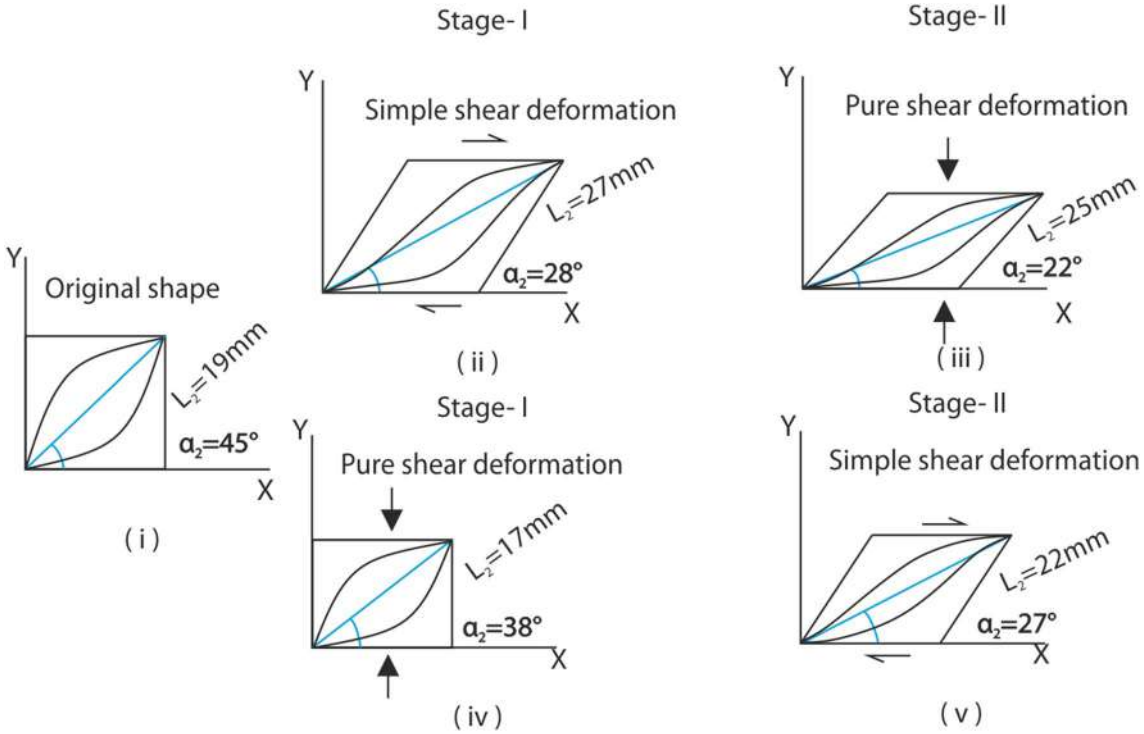

Fig. 7 Response of a square block under pure and simple shear (ten Grotenhuis et al. 2003) changes shape of a square. L_2 lengthens and α_2 reduces subsequently. **i** Square block with L_2 value 19 mm and α_2 value 45°. **ii** Initial phase of simple shear deformation leads increasing length of L_2 and decreasing the angle α_2. **iii** Final phase of pure shear deformation denotes decrease in the length of $L_2 = 25$ mm and decreasing the angle $\alpha_2 = 22°$. **iv** Initial phase of pure shear deformation leads decreasing length of L_2 and decreasing the angle α_2. **v** Final phase of non-coaxial shear deformation denotes increase in the length of $L_2 = 22$ mm and decreasing the angle $\alpha_2 = 27°$

P- and *S*-, are of low λ (Fig. 10i, Type-I vs. Type-III) and high wavelength. Significant difference in L_2 and L_3 value (Fig. 10i, Type-III) indicates a greater curvature (high amplitude, Fig. 10i with $m_1n_1 < m_2n_2 < m_3n_3$), complimented by relatively high L_1 values (Fig. 10i, Type-III). From Type-I to Type-III, as the value of L_1 increases, the difference between L_2 and L_3 magnitude also increases. Figures 10i–iii show increasing curvature from Type-I to Type-III with significant rise of L_1 value along with minor increase of L_2 and L_3 value.

Good correlations for α_2 vs. α_3 ($R^2 = 0.69$), and $(\alpha_3 - \alpha_1)$ vs. $(\alpha_1 - \alpha_2)$ ($R^2 = 0.75$) suggest that the curve segments are of 180° rotational symmetry. Note Farrell and Shepard (1981) coined the term "180° rotational symmetry". In Fig. 10ii, Type-I, II and III sigmoids have curve segment '*r*', which after 180° rotation becomes the segment 's'. In Fig. 10ii, Type-IV sigmoids do not achieve such a rotational symmetry. There the segments '*r*' and '*s*' are of different shapes. This is also reflected in terms of poor correlations between α_2 vs. α_3 and $(\alpha_3 - \alpha_1)$ vs. $(\alpha_1 - \alpha_2)$.

Rigid body rotation of the sigmoid curves, if attained by ductile shear, can increase or decrease α_1, α_2 and α_3 individually, however, the difference between the angle remain

Table 2 First-order linear correlation between parameters (L_1, L_2, L_3, α_1, α_2 and α_3)

Sr. no	Correlation type ('*'):poor correlation; ('^'):moderate-good correlation)	*Y*-Axis	*X*-Axis	Linear correlation between parameters (L_1, L_2, L_3, α_1, α_2 and α_3)represented by straight line equation ($y=Ax+B$)		R^2
				A	*B*	
First-order plots						
1	^	L_3	L_1	1.1787	4.8868	0.5211
2	^	L_2	L_3	1.2471	1.2398	0.927
3	^	L_1	L_2	0.3652	− 0.2633	0.5966
4	^	α_2	α_3	0.6689	3.006	0.6999
5	*	α_2	L_2	− 0.0203	34.375	0.0003

unaffected and such rotated curves retain original shapes and sizes. For example, in Fig. 10iv, the acute angles (α_i, $i=1$, 2, 3) of Type-I sigmoid are 23.5°, 60° and 65°, respectively. After 38.25° clockwise rotation, the acute angles change to − 14.75°, 21.75° and 26.75°, respectively (Fig. 10iv; Type-I). The negative angle indicates an anti-clockwise measurement form the *X*-axis. The difference between the individual acute angle remain constant i.e. $\alpha_1-\alpha_2=36.5°$; $\alpha_3-\alpha_2=5°$. This leads to retain the shape and provides no influence on angle ratio plots (Fig. 11).

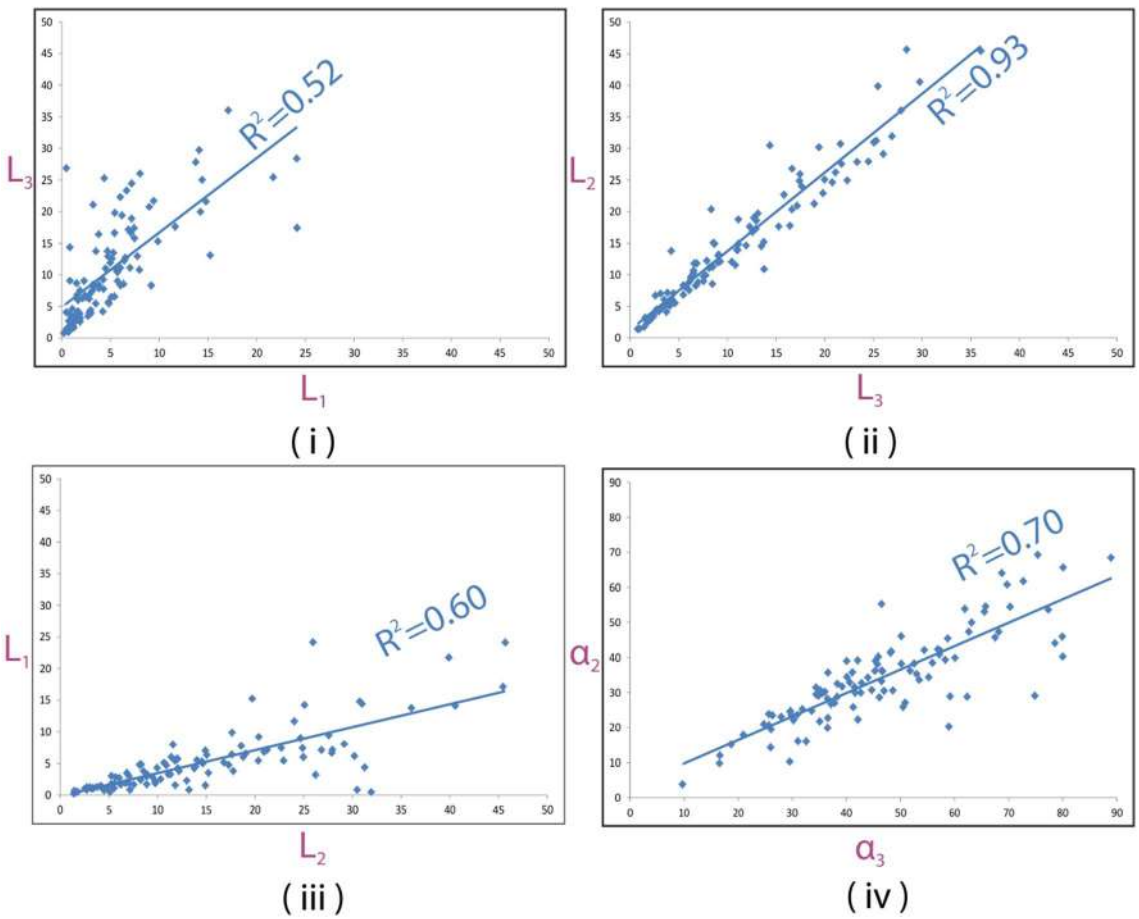

Fig. 8 Different types of first-order scatter plots (one to one parameter comparison) of natural sigmoids defined by *P*- and *S*- shear planes plotted from NW Lesser Indian Himalaya. Detail at the "Results" section. **i** L_3 vs. L_1, **ii** L_2 vs. L_3, **iii** L_1 vs. L_2, **iv** α_2 vs. α_3

Table 3 Second-order linear correlation between parameters (L_1, L_2, L_3, α_1, α_2 and α_3)

Sr. no	Correlation type ('*'):poor correlation; ('^'):moderate-good correlation)	*Y*-Axis	*X*-Axis	Linear correlation between parameters (L_1, L_2, L_3, α_1, α_2 and α_3) represented by straight line equation ($y=Ax+B$)		R^2
				A	*B*	
Second order plots						
1	^	$\alpha_3\_\alpha_1$	$\alpha_1\_\alpha_2$	− 0.9211	14.446	0.7503

Relation between sigmoid geometries & regional structures

Refer to Appendix 1 for background information. The *P*- and the *S*-planes situated within ~ 2 km range of the regional structure (e.g., in Fig. 2 location point: 5- Munsiari Thrust, 15 and 25- Berinag Thrust, 46- Tons Thrust, 50- Aglar Thrust, 75-Mussoorie syncline etc.) display comparatively poor correlation amongst the chosen parameters (e.g., L_3 vs. L_1, $R^2=0.26$; L_2 vs. L_3, $R^2=0.88$; L_1 vs. L_2, $R^2=0.31$; α_2 vs. α_3, $R^2=0.65$). Plots associated with the observed P- and S-planes situated > 2 km away from the regional faults and fold axes give a comparatively stronger linear fit (e.g., L_3 vs. L_1, $R^2=0.71$; L_2 vs. L_3, $R^2=0.94$; L_1 vs. L_2, $R^2=0.81$; α_2 vs. α_3, $R^2=0.81$). Only the plot of $(\alpha_3\_\alpha_1)$ vs. $(\alpha_1-\alpha_2)$ in which shear fabrics are encountered > 2 km away from regional structures

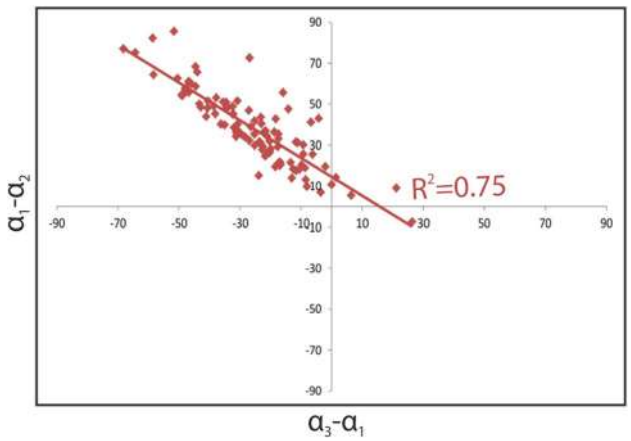

Fig. 9 Second-order scatter plots (individual parameters are combined together) of natural sigmoid defined by *P*- and *S*- shear planes. Details are discussed in the "Results" section. **i** $(\alpha_3-\alpha_1)$ vs. $(\alpha_1-\alpha_2)$

$[(\alpha_3\_\alpha_1)$ vs. $(\alpha_1\_\alpha_2)$, $R^2=0.79]$ display slightly better correlation than the shear fabrics encountered at < 2 km away from regional structure $[(\alpha_3\_\alpha_1)$ vs. $(\alpha_1\_\alpha_2)$, $R^2=0.74]$ (sl no.10 in Table 4).

Relation between sigmoid geometries & lithology

Difference in grain size (Bose et al. 2018), mineralogy (Libak et al. 2019) in micro-scale and even the cement composition within carbonates (Steen and Andresen, 1999) play vital roles in altering meso-micro scale fault and shear fabric geometries. Bastesen and Braathen (2010) explained the effect of lithologic composition over the fault geometry.

Plots showing good correlations (e.g., L_3 vs. L_1, L_2 vs. L_3, L_1 vs. L_2, α_2 vs. α_3, $(\alpha_3\_\alpha_1)$ vs. $(\alpha_1-\alpha_2)$ are further categorized based on lithology (Fig. 12) in which the *P*- and the *S*-planes are observed. Amongst these, the L_3 vs. L_1, and the α_2 vs. α_3 plots suggest *P*- and *S*-planes in politic rocks from the Rautgara Formation slates/schists and Chandpur Formation slates/schists develop at a low-angle with *Y*- and *S*- planes, and the sigmoids are flatter with high amplitude (Fig. 10iii, Type-I). On the other hand, psammitic rocks (Rautgara quartzite, Nagthat quartzite and Berinag quartzite) reveal a comparatively high-angle relation between *Y*- and *P*- plane, and *S*- and *C*-planes with sigmoids of relatively low-amplitudes (Fig. 10iii, Type-I). For limestones (Krol Limestone), conglomerates (Blaini Formation) and the MCT Zone schists along with along with quartzites (Berinag, Nagthat, Rautgara and Chandpur Formation), the graphs (Fig. 12i) suggest that most of the sigmoids are the Type-II varieties.

The parameter α_2 was plotted against lithology (Repository Fig. 4 in ESM). Majority of the α_2 values range in between 20° and 50° in case of quartzite with maximum ranging 30°–40°, Schist/slates, MCT schists and limestones cover a wider range of α_2 with a majority between 20° and 30°. α_2 in conglomerate ranges 20°–50°. Range of α_2 may indicate different degrees of non-coaxial shear.

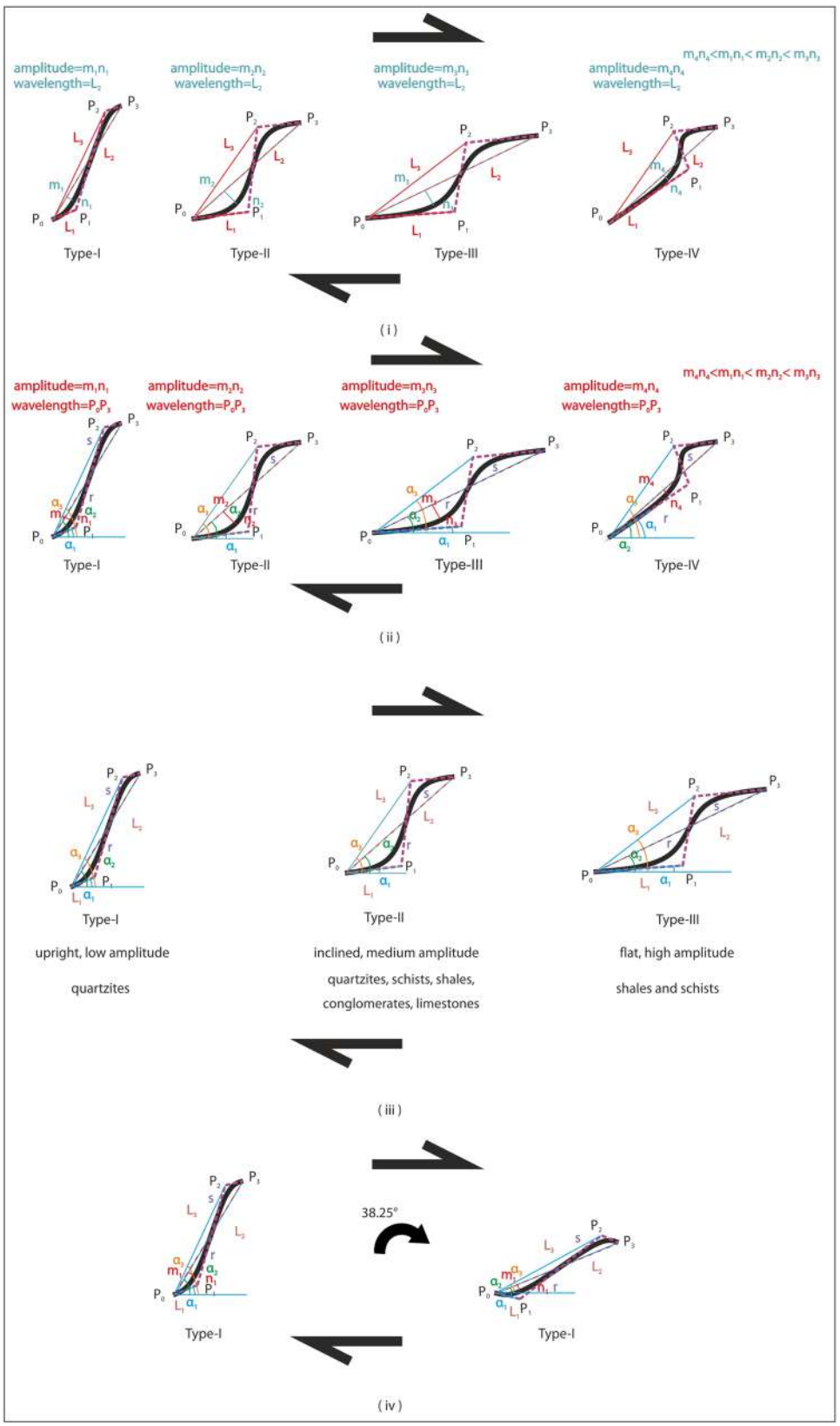

Fig. 10 Different types of sigmoid shapes. Moving towards right, the end point location P_3 also moves. Simultaneously P_1 and P_2 modify their locations. P_0 end point location remains fixed. Sense of slip: top-to-right. P_0, P_1, P_2, and P_3 are the control points and jointed by violet dashed lines. Amplitude and wavelength increase towards right. **i** L_1, L_2 and L_3 are marked by red solid lines. L_1 significantly increase towards right. **ii** α_1, α_2 and α_3 are represented by blue, green and orange, respectively and are identified by blue solid lines. From Type-I to Type-III, α_1, α_2 and α_3 reducebut preserves the 180° rotational symmetry (after 180° rotation, the curve segment '*r*' becomes curve segment '*s*', and vice versa). Type-IV is an asymmetric sigmoid, segment '*r*' is unequal to the segment '*s*'. Amplitude of Type-IV sigmoid is less than all other types, in Type-III it is maximum. Difference in behaviour in ductile and brittle regimes are not accounted. **iii** Sigmoid geometries in different lithology. **Type-I:** Lithology plots reveal small L_1 value along with high values of α_2 and α_3 is dominantly represented by psammitic composition of rocks. **Type-III:** Considerably high L_1 value along with low values of α_2 and α_3 represented by pelitic composition. **Type-II:** Most common type of sigmoid in the field and covers a wide range of lithology (e.g., quartzites, schists, limestones and conglomerates and MCT zone schists). **iv** Schematic example of retention in geometry, even after 38.25° clockwise block rotation of Type-I sigmoid. Individual angular differences (e.g., α_3–α_2, α_2–α_1) remain unaffected even after block rotation

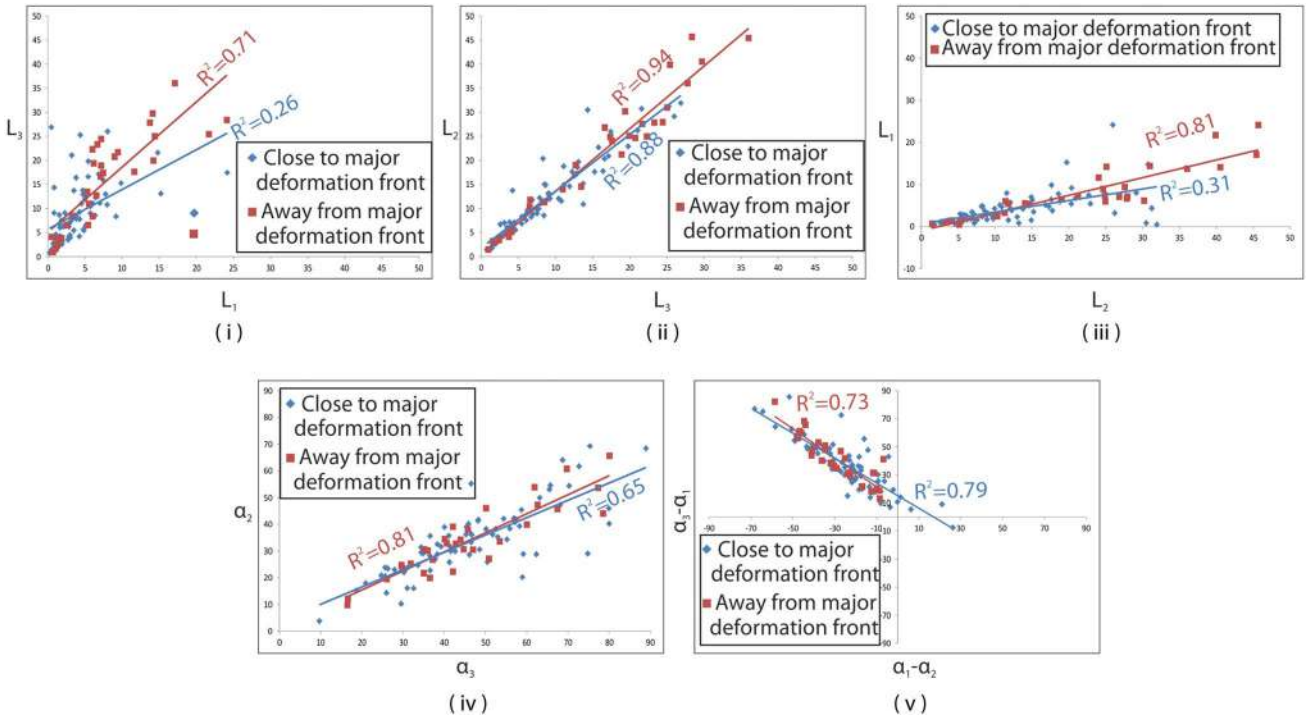

Fig. 11 Scatter plots showing $R^2 \geq 0.5$; correlations are further divided based on the existence of regional structures such as folds or faults within ~2 km on the road-section. Red square: sigmoids belonging from NW Lesser Indian Himalaya, developed > ~2 km away from regional structure; blue diamond: sigmoids developed < ~2 km away from the regional structure. Details at "Discussions" section. **i** L_3 vs. L_1, **ii** L_2 vs. L_3, **iii** L_1 vs. L_2, **iv** α_2 vs. α_3, **v** $(\alpha_3-\alpha_1)$ vs. $(\alpha_1-\alpha_2)$

Table 4 Impact of regional structure over *P*- & *S*-plane geometry

Sr. no	Distance between regional structure & *P*- & *S*-plane (a) (< ~2 km distance) (b) (> ~2 km distance)	*Y*-Axis	*X*-Axis	Linear correlation between parameters (L_1, L_2, L_3, α_1, α_2 and α_3) represented by straight line equation ($y=Ax+B$)		R^2
				A	*B*	
1	a	L_3	L_1	0.826	5.6891	0.2609
2	b	L_3	L_1	1.3541	5.0521	0.7096
3	a	L_2	L_3	1.1787	1.7987	0.8814
4	b	L_2	L_3	1.3011	0.5485	0.9483
5	a	L_1	L_2	0.2746	0.6914	0.311
6	b	L_1	L_2	0.4197	0.9747	0.8124
7	a	α_2	α_3	0.6491	3.8439	0.6525
8	b	α_2	α_3	0.7127	1.1815	0.8123
9	a	$\alpha_3 - \alpha_1$	$\alpha_{1\_}\alpha_2$	− 1.358	11.034	0.7949
10	b	$\alpha_3 - \alpha_1$	$\alpha_{1\_}\alpha_2$	− 0.8894	15.261	0.7356

Conclusions

Geometric matching of NURB curve in 2D (Piegl and Tiller 1997) involves its two segments combined to a sigmoid shape. In this study, *P*-planes and *S*-planes photographed in the field are imported and visually matched in the program by drawing curves using the B-spline tool. The process is simple, quick and the results can be plotted as 2D scatter plots. NURB curves can be modified locally unlike the Bézier curves. NURB offers a wider range of curves, from flat to pointy, without changing the degree of the polynomial function.

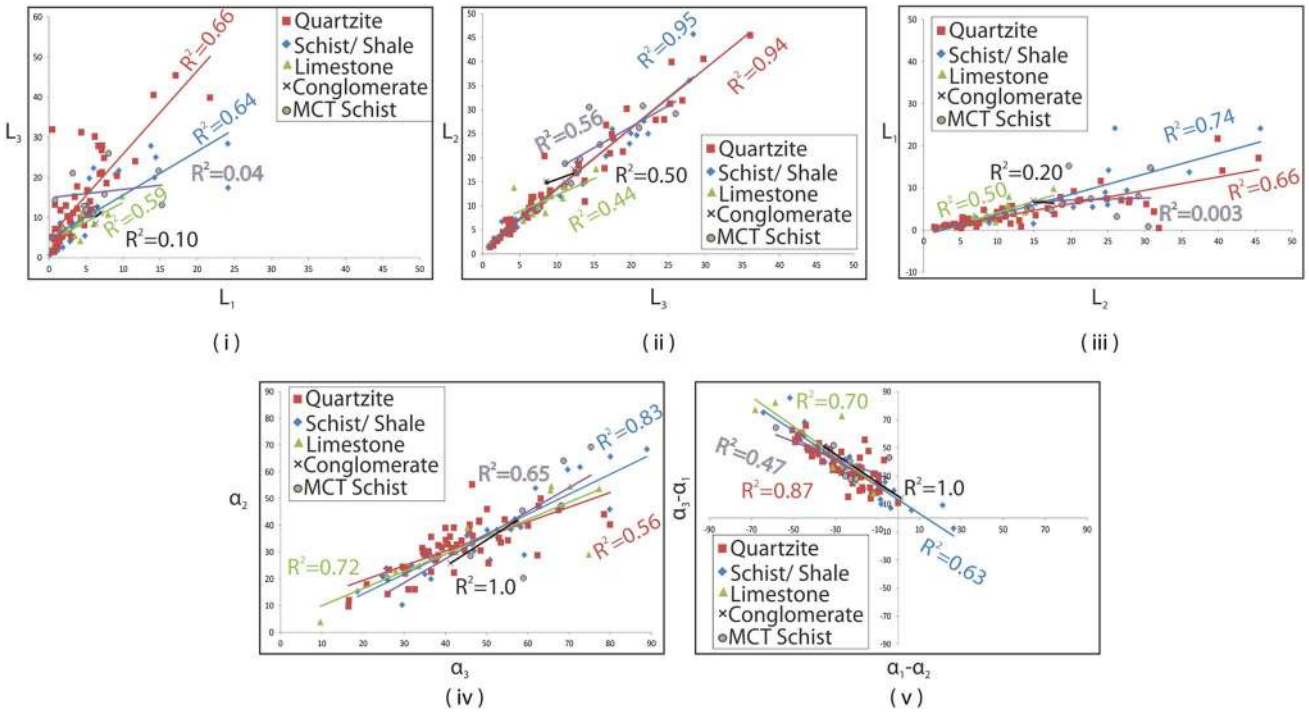

Fig. 12 Scatter plots showing $R^2 \geq 0.5$; correlations divided based on litho-types. **a** Schistose/Slate rocks (red square), **b** Quartzites (blue diamond), **c** Limestones (green triangle), **d** Conglomerates (violet cross) from the LH. Detailed in "Discussions" section. **i** L_3 vs. L_1, **ii** L_2 vs. L_3, **iii** L_1 vs. L_2, **iv** α_2 vs. α_3, **v** $(\alpha_3-\alpha_1)$ vs. $(\alpha_1-\alpha_2)$

This study utilizes a total of 103 curves recorded mostly along the Bhagirathi section of the LH starting from ~ 10 NE of Uttarkashi up to Mussoorie. Field photographs of *P*- and *S*- plane are reproduced using the B-spline tool in the Rhinoceros software 5 SR Service (free trial version). The visually matched curves are defined using six shape parameters (L_1, L_2, L_3, α_1, α_2 and α_3). With progressive simple shear, within all types of sigmoid, values of L_2 ideally increase and that of α_2 decrease (ten Grotenhuis et al. 2003; Fig. 7). However, any direct relation between α_2 and L_2 could not be established ($R^2 = 0.0003$) due to different sizes of the sigmoids identified in the field. This would mean that at the starting point of deformation, the proto-*P* and *S*-planes were of different sizes.

However, some distinct observations are made upon further analysis which involves relation between wavelength and amplitude. Good correlations between L_3 vs. L_1, L_2 vs. L_3 and L_1 vs. L_2 plots suggest that all types of sigmoids are overall of low amplitude and high wavelength. Since the sigmoids in the field are of variable sizes and shapes, individual magnitudes of L_3, L_1 and L_2 become insignificant. Length ratios (L_3:L_1, L_2:L_3 and L_1:L_2) in scatter plots differentiates different types of sigmoids (Fig. 10: Type-I vs. Type-III). These similarities roughly stipulate that the regional structures (e.g., Munsuari Thrust, Berinag Thrust, Main Boundary Thrust etc.) can have considerable influence on the development of shear fabrics around them.

Relation between sigmoid geometry and lithology, e.g., slates and schist and slates of Rautgara Formation and Chandpur Formation, reveals that the sigmoids are flatter (with low α_2 and α_3 value (Fig. 12iv); low-angle between *P*- and *S*- plane with *Y* and *C*-planes, respectively) along with high-amplitude with relatively high L_1 value (Fig. 12i).

These are the Type-III sigmoid (Fig. 10iii). Sigmoids developed within the Rautgara, Nagthat and Berinag quartzites are upright (with high α_2 and α_3 values, Fig. 12iv). High-angle between *P*- (and *S*-) plane with the *Y* (and *C*-) planes are characterized by low amplitudes with relatively low L_1 values (Fig. 12i) than the Type-I sigmoid within the pelitic rocks (Fig. 10iii). With this observation, sigmoids documented with the LH schists, quartzites and slates can be categorized as the Type-I and II varieties (Fig. 10i). The Type-I *v*arieties are of low amplitude whereas amplitude increases significantly in the Type-III sigmoids in quartzites, schists and slates (Fig. 10i). L_3 vs. L_1 and α_2 vs. α_3 plots (Figs. 12i, iv) suggests that the Type-II sigmoids within the Krol limestones, the conglomerates of the Blaini Formation and MCT zone schists are of relatively moderate amplitudes along with relatively moderate wavelengths (Fig. 10iii). This stipulates favourable tectonic regimes for the development of extensional- and compressional shear fabrics. Pelitic and

psammitic rock compositions show distinct L_3 vs. L_1 and α_2 vs. α_3 plots. Type-I sigmoids are found mainly from the psammitic rocks, whereas the Type-III mainly from the pelitic variety.

Appendix 1

Pre-existing regional structures distribute and orient subsequent structures (Misra and Mukherjee 2015; Fossen et al. 2017). For example, taper geometry of the sediment pile, litho-tectonic stratigraphy and overall margin of the shelf influenced the fold-thrust belt in the Cordilleran sedimentary basin (Mitra 1997). Earlier developed compressional structures in the Alpine Corsica affected the geometry of later developed extensional structures (Jolivet et al. 1991).

Balda et al. (1995) argued orogen-parallel deformation (extension) to be a syn-collisional product as documented form the Variscan Belt. In the Western Coast Belt, orogen-perpendicular shortening shares syn-kinematic relationship with orogen-parallel extension recorded from conjugate shear during the mid-Cretaceous (Angen et al. 2014).

These ideas from other orogens lead us to evaluate the possibility of impact of regional structures (e.g., Munsuari Thrust, Berinag Thrust, Singuini Thrust, Dharasu Thrust, Tons Thrust, Basul Thrust, Deosari syncline, Aglar Thrust, Mussoorie syncline, Kathu-ki-chail Thrust, Main Boundary Thrust) over the geometries of the smaller scale P- and S- shear planes.

Supplementary Information The online version contains supplementary material available at https://doi.org/10.1007/s00531-022-02159-4.

Acknowledgements Part of the Ph.D. thesis of TB (Biswas, submitted). Research Progress Committee members Profs. G.N. Jadhav and P. Naraga (IIT Bombay) raised many useful comments. Fieldwork was conducted with IIT Bombay's CPDA grant provided to SM. Narayan Bose (IIT Kharagpur) assisted in fieldwork. Wolf-Christian Dullo (Chief Editor), Associate Editor, and the Managing Editor (Monika Dullo) are thanked. Lucie Novakova (reviewer) and an anonymous reviewer provided detail critical comments in three rounds.

References

Agarwal NC, Kumar G (1973) Geology of the upper Bhagirathi and Yamuna valleys, Uttarkashi district, Kumaun Himalaya. Himal Geol 3:2–23

Agarwal A, Agarwal KK, Bali R, Prakash C, Joshi G (2016) Back-thrusting in Lesser Himalaya: evidences from magnetic fabric studies in parts of Almora Crystalline Zone, Kumaun Lesser Himalaya. J Earth Syst Sci 125:873–884

Ahlgren SG (2001) The nucleation and evolution of Riedel shear zones as deformation bands in porous sandstone. J Struct Geol 23:1203–1214

Akram MS, Farooq S, Naeem M, Ghazi S (2017) Prediction of mechanical behaviour from mineralogical composition of Sakesar limestone, Central Salt Range, Pakistan. Bull Eng Geol Env 76:601–615

Anders MH, Laubach SE, Scholz CH (2014) Microfractures: a review. J Struct Geol 69:377–394

Angen JJ, Van Staal CR, Lin S, Nelson JL, Mahoney JB, Davis DW, McClelland WC (2014) Kinematics and timing of shear zone deformation in the western Coast Belt: evidence for mid-Cretaceous orogen-parallel extension. J Struct Geol 68:273–299

Balda MD, Catalán JM, Arribas PA (1995) Syn-collisional extensional collapse parallel to the orogenic trend in a domain of steep tectonics: the Salamanca Detachment Zone (Central Iberian Zone, Spain). J Struct Geol 17:163–182

Barazzetti L, Banfi F, Brumana R, Roncoroni F, Previtali M (2016) BIM from laser scans… not just for buildings: NURBS-based parametric modeling of a medieval bridge. In: XXIII ISPRS Congress, Commission V (pp 51–56)

Bastesen E, Braathen A (2010) Extensional faults in fine grained carbonates–analysis of fault core lithology and thickness–displacement relationships. J Struct Geol 32:1609–1628

Biswas T, Bose N, Dutta D, Mukherjee S (2021) Arc-parallel shears in collisional orogens: global review and paleostress analyses from the NW Lesser Himalayan Sequence (Garhwal region, Uttarakhand, India). Mar Petrol Geol 128:1–20

Bose N, Mukherjee S (2019a) Field documentation and genesis of the back-structures rom the Garhwal Lesser Himalaya, Uttarakhand, India. In: Sharma R, Villa IM, Kumar S (eds) Crustal architecture and evolution of the Himalaya–Karakoram–Tibet Orogen. Geological Society, London, Special Publications, vol 481, pp 111–125

Bose N, Mukherjee S (2019b) Field documentation and genesis of back-structures in ductile and brittle regimes from the foreland part of a collisional orogen: examples from the Darjeeling-Sikkim Lesser Himalaya, India. Int J Earth Sci 108:1333–1350

Bose N, Dutta D, Mukherjee S (2018) Role of grain-size in phyllonitisation: insights from mineralogy, microstructures, strain analyses and numerical modeling. J Struct Geol 112:39–52

Catlos EJ, Harrison TM, Manning CE, Grove M, Rai SM, Hubbard MS, Upreti BN (2002) Records of the evolution of the Himalayan orogen from in situ Th–Pb ion microprobe dating of monazite: Eastern Nepal and western Garhwal. J Asian Earth Sci 20:459–479

Célérier J, Harrison TM, Webb AAG, Yin A (2009) The Kumaun and Garwhal lesser Himalaya, India: part 1. Structure and stratigraphy. Geol Soc Am Bull 121:1262–1280

Cox MG (1972) The numerical evaluation of B-splines. J Inst Math & App 10:134–149

Davis BK, Blewett RS, Squire R, Champion DC, Henson PA (2010) Granite-cored domes and gold mineralisation: Architectural and geodynamic controls around the Archaean Scotia-Kanowna Dome, Kalgoorlie Terrane, Western Australia. Precambr Res 183:316–337

De Boor C (1972) On calculating with B-splines. J Approx Theory 6:50–62

de Kemp EA, Sprague KB (2003) Interpretive tools for 3-D structural geological modeling part I: Bezier-based curves, ribbons and grip frames. GeoInformatica 7:55–71

Dubey AK (2014) Understanding an orogenic belt. Springer, Heidelberg, New York, Dordrecht, London

Dutta D, Mukherjee S (2019) Opposite shear senses: geneses, global occurrences, numerical simulations and a case study from the Indian western Himalaya. J Struct Geol 126:357–392

Edwards MA, Harrison TM (1997) When did the roof collapse? Late Miocene north-south extension in the high Himalaya revealed by Th-Pb monazite dating of the Khula Kangri granite. Geology 25:543–546

Evans KR, McKenna LW, Lieberman BS, Weichert WD, Macleod KG (2018) Geology of the Nelson limestone, Postelnunatak, Patuxent range, Antarctica. Antarct Sci 30:29–43

Farrell JE, Shepard RN (1981) Shape, orientation, and apparent rotational motion. J Exp Psychol Hum Percept Perform 7:477

Fisher RS (1995) Geologic, geochemical, and geographic controls on NORM in produced water from Texas oil, gas, and geothermal reservoirs. In: SPE/EPA Exploration and Production Environmental Conference. Society of Petroleum Engineers

Fossen H (2016) Structural geology. Cambridge University Press, Cambridge

Fossen H, Soliva R, Ballas G, Trzaskos B, Cavalcante C, Schultz RA (2017) A review of deformation bands in reservoir sandstones: geometries, mechanisms and distribution. Geol Soc Lond Spec Publ 459:9–33

Francké JC, Yelf R (2003) Applications of GPR for surface mining. In: Proceedings of the 2nd international workshop on advanced ground penetrating radar, IEEE, pp 115–119

Gabrielli CP, McDonnell JJ (2020) Modifying the Jackson index to quantify the relationship between geology, landscape structure, and water transit time in steep wet headwaters. Hydrol Process 34:2139–2150

Gogoi MP, Mukherjee S, Goswami TK (2017) Analyses of fold profiles by changing weight parameters of NURB curves. J Earth Syst Sci 126:98

Gogoi MP, Mukherjee S (2019) Synthesis of Folds in 3D with Bézier-Surface. In: Developments in structural geology and tectonics, vol 5, pp 279–290, Elsevier

Gudmundsson A (2011) Rock fractures in geological processes. Cambridge University Press, Cambridge

Hintersberger E, Thiede RC, Strecker MR (2011) The role of extension during brittle deformation within the NW Indian Himalaya. Tectonics 2011:30

Hudleston PJ, Treagus SH (2010) Information from folds: a review. J Struct Geol 32:2042–2071

Huisman DJ, Vermeulen FJH, Baker J, Veldkamp A, Kroonenberg SB, Klaver GT (1997) A geological interpretation of heavy metal concentrations in soils and sediments in the southern Netherlands. J Geochem Explor 59:163–174

Jacquemyn C, Jackson MD, Hampson GJ (2019) Surface-based geological reservoir modelling using grid-free NURBS curves and surfaces. Math Geosci 51:1–28

Jain AK (1971) Stratigraphy and tectonics of lesser Himalayan region of Uttarkashi, Garhwal Himalaya. Himalayan Geol 1:25–58

Jain AK (1987) Kinematics of the transverse lineaments, regional tectonics and Holocene stress field in the Garhwal Himalaya. J Geol Soc India 30:169–186

Jolivet L, Daniel JM, Fournier M (1991) Geometry and kinematics of extension in Alpine Corsica. Earth Planet Sci Lett 104:278–291

Koerber C, Möller DPF, Kesper B, Hansmann W (2003) A 4D modelling concept using NURBS applied to geosciences. In: Proceedings IV. IMACS Symposium on Mathematical Modelling, Vienna

Li W, Liu S, Wang Y, Qian T, Gao T (2017) Duplex thrusting in the South Dabashanarcuate belt, central China. J Struct Geol 103:120–136

Libak A, Torabi A, Alaei B (2019) Normal fault geometric attribute variations with lithology: examples from the Norwegian Barents Sea. Geol Soc Lond Spec Publ 495:SP495-2018

Liu C, Zhang Y, Wang Y (2009a) Analysis of complete fold shape based on quadratic Bézier curves. J Struct Geol 31:575–581

Liu C, Zhang Y, Shi B (2009b) Geometric and kinematic modeling of detachment folds with growth strata based on Bézier curves. J Struct Geol 31:260–269

Mahato S, Mukherjee S, Bose N (2019) Documentation of brittle structures (back shear and arc-parallel shear) from Sategal and Dhanaulti regions of the Garhwal Lesser Himalaya (Uttarakhand, India). In: Mukherjee S (ed) Tectonics and structural geology: Indian context, pp 411–423

Maynard JB (1992) Chemistry of modern soils as a guide to interpreting Precambrian paleosols. J Geol 100:279–289

Meigs AJ, Burbank DW, Beck RA (1995) Middle-late Miocene (> 10 Ma) formation of the Main Boundary thrust in the western Himalaya. Geology 23:423–426

Metcalfe RP (1993) Pressure, temperature and time constraints on metamorphism across the Main Central Thrust zone and High Himalayan Slab in the Garhwal Himalaya. Geol Soc Lond Spec Publ 74:485–509

Meyer SE, Kaus BJ, Passchier C (2017) Development of branching brittle and ductile shear zones: a numerical study. Geochem Geophys Geosyst 18:2054–2075

Misra AA, Mukherjee S (2015) Tectonic inheritance in continental rifts and passive margins. In: Springerbriefs in Earth Sciences. ISBN 978-3-319-20576-2

Mitra G (1997) Evolution of salients in a fold-and-thrust belt: the effects of sedimentary basin geometry, strain distribution and critical taper. In: Evolution of geological structures in micro-to macro-scales (pp 59–90). Springer, Dordrecht

Montemagni C, Carosi R, Fusi N, Iaccarino S, Montomoli C, Villa IM, Zanchetta S (2020) Three-dimensional vorticity and time-constrained evolution of the Main Central Thrust zone, Garhwal Himalaya (NW India). Terra Nova 32:215–224

Mukherjee S (2011) Mineral fish: their morphological classification, usefulness as shear sense indicators and genesis. Int J Earth Sci 100:1303–1314

Mukherjee S (2013) Deformation microstructures in rocks. Springer Science & Business Media, Berlin

Mukherjee S (2017) Review on symmetric structures in ductile shear zones. Int J Earth Sci 106:1453–1468

Mukherjee S, Koyi HA (2010) Higher Himalayan Shear Zone, Zanskar Indian Himalaya: microstructural studies and extrusion mechanism by a combination of simple shear and channel flow. Int J Earth Sci 99:1083–1110

Mukhopadhyay DK, Mishra P (2005) A balanced cross section across the Himalayan frontal fold-thrust belt, Subathu area, Himachal Pradesh, India: thrust sequence, structural evolution and shortening. J Asian Earth Sci 25:735–746

Nabavi ST, Fossen H (2021) Fold geometry and folding—a review. Earth-Sci Rev 222:103812

Nagy C, Godin L, Antolín B, Cottle J, Archibald D (2015) Mid-Miocene initiation of orogen-parallel extension, NW Nepal Himalaya. Lithosphere 7:483–502

Paluszny A, Matthäi SK, Hohmeyer M (2007) Hybrid finite element–finite volume discretization of complex geologic structures and a new simulation workflow demonstrated on fractured rocks. Geofluids 7:186–208

Passchier CW, Trouw RAJ (2005) Microtectonics, 2nd edn. Springer, Berlin

Patel RC, Singh P, Lal N (2015) Thrusting and back-thrusting as post-emplacement kinematics of the Almora klippe: Insights from Low-temperature thermochronology. Tectonophysics 653:41–51

Peacock DCP, Sanderson DJ, Rotevatn A (2018) Relationships between fractures. J Struct Geol 106:41–53

Piegl L, Tiller W (1997) Symbolic operators for NURBS. Comput Aided Des 29:361–368

Ponce C, Druguet E, Carreras J (2013) Development of shear zone-related lozenges in foliated rocks. J Struct Geol 50:176–186

Prautzsch H, Boehm W, Paluszny M (2002) Bézier and B-spline techniques. Springer Science & Business Media, Berlin

Renard P, Courrioux G (1994) Three-dimensional geometric modeling of a faulted domain: the Soultz Horst example (Alsace, France). Comput Geosci 20:1379–1390

Sonder LJ (2001) Ductile shear zones as counterflow boundaries in pseudoplastic fluids: discussion and theory. J Struct Geol 23:149–153

Sprague KB, De Kemp EA (2005) Interpretive tools for 3-D structural geological modelling part II: surface design from sparse spatial data. GeoInformatica 9:5–32

Steen Ø, Andresen A (1999) Effects of lithology on geometry and scaling of small faults in Triassic sandstones, East Greenland. J Struct Geol 21:1351–1368

Ten Grotenhuis SM, Trouw RAJ, Passchier CW (2003) Evolution of mica fish in mylonitic rocks. Tectonophysics 372:1–21

Thakur VC, Joshi M, Sahoo D, Suresh N, Jayangondapermal R, Singh A (2014) Partitioning of convergence in Northwest Sub-Himalaya: estimation of late Quaternary uplift and convergence rates across the Kangrareentrant, North India. Int J Earth Sci 103:1037–1056

Thiede RC, Arrowsmith JR, Bookhagen B, McWilliams MO, Sobel ER, Strecker MR (2005) From tectonically to erosionally controlled development of the Himalayan orogen. Geology 33:689–692

Torabi A, Alaei B, Libak A (2019) Normal fault 3D geometry and displacement revisited: insights from faults in the Norwegian Barents Sea. Mar Pet Geol 99:135–155

Vannay JC, Grasemann B, Rahn M, Frank W, Carter A, Baudraz V, Cosca M (2004) Miocene to Holocene exhumation of metamorphic crustal wedges in the NW Himalaya: evidence for tectonic extrusion coupled to fluvial erosion. Tectonics 23:1

Yin A (2006) Cenozoic tectonic evolution of the Himalayan orogen as constrained by along-strike variation of structural geometry, extrusion history, and foreland sedimentation. Earth Sci Rev 76:1–131

Zhong DH, Li MC, Song LG, Wang G (2006) Enhanced NURBS modeling and visualization for large 3D geoengineering applications: an example from the Jinping first-level hydropower engineering project, China. Comput Geosci 32:1270–1282

Zhong D, Li M, Wang G, Wei H (2004) NURBS-based 3D graphical modeling and visualization of geological structures. In: Third international conference on image and graphics (ICIG'04), IEEE (pp 414–417)